Science
AAAS

Supplementary Materials for

Cryo-EM structures of AMPA receptor in complex with its auxiliary subunit cornichon

T. Nakagawa
Correspondence to: terunaga.nakagawa@vanderbilt.edu

This PDF file includes:

Extended text
Materials and Methods
Figs. S1 to S18
Table S1
References #1-24

The following Supplementary Materials for this manuscript will be available:

Cryo-EM density maps

(1) **A2C3-AS**: Map of the full-length GluA2-CNIH3 complex in asymmetric conformation (AS) at 4.4Å resolution
(2) **A2C3-PS**: Map of the full-length GluA2-CNIH3 complex in pseudo-symmetric conformation (PS) at 4.4Å resolution
(3) **NTD(AS)**: Map (C1) of the NTD derived from particles in AS at an overall resolution of 3.1Å.
(4) **LBD-TMD-C3(AS)I**: Map (C1) of the LBD-TMD-C3 derived from particles in AS at an overall resolution of 3.5Å.
(5) **LBD-TMD-C3(AS)II**: Map (C2) of the LBD-TMD-C3 derived from particles in AS at an overall resolution of 3.3Å.
(6) **NTD(PS)**: Map (C2) of the NTD derived from particles in PS at an overall resolution of 3.1Å.
(7) **LBD-TMD-C3(PS)**: Map (C2) of the LBD-TMD-C3 derived from particles in PS at an overall resolution of 3.2Å.
(8) **LBD-TMD-C3**: Map (C2) of the LBD-TMD-C3 derived from combining datasets of AS and PS at an overall resolution of 3.0Å. This map and the following map contain the highest quality density of TMD and CNIH3.
(9) **LBD-TMD-C3$_{\text{lipid}}$:** Map (C2) of the LBD-TMD-C3 calculated by imposing C2 symmetry in all steps. The map is generated from a fewer number of particles than

map LBD-TMD-C3 and resolves the lipid like density at higher quality. The overall resolution is 3.3Å.

The atomic coordinates built from the corresponding EM density map
(10) NTD(AS)
(11) NTD(PS)
(12) LBD-TMD-C3(AS) II
(13) LBD-TMD-C3(PS)
(14) LBD-TMD-C3
(15) LBD-TMD-$C3_{\text{lipid}}$

Extended text

Expression, purification, and functional validation of GluA2/CNIH3 complex

The isoform of rat GluA2 used in this study is the *flip* splice variant with an edited pore at the Q/R site (residue 586). GluA2 and CNIH3 were stably co-expressed in a HEK cell line with a DOX inducible system to minimize toxicity caused by activation of the ion channel (FigS1A). A slow desensitizing peak with a large steady state component was observed when channel activity was recorded using fast glutamate application, indicating that the expressed complex is functional (FigS1B). The complex was first dissolved in detergent and purified to homogeneity (see methods and FigS1C).

Cryo-EM and image processing

The cryo-EM micrographs of A2-C3 bound to antagonist ZK200775 (280µM) contained well-defined mono-dispersed particles (FigS2). Over 11,000 images were recorded using the Gatan K3 direct electron detector. The overview of image processing is provided in FigS3. In the initial phase, during which greater number of particles was handled, the images were binned by 2-fold (2.132Å/pixel) to optimize the computational cost. In particular, the first 3D classification specifying four classes without imposing symmetry was conducted using binned images. Two classes produced the AS and PS conformations, which were further refined to an overall resolution of 4.4Å. Further sub-classification and refinement of full-length AS and PS did not significantly improve resolution.

To improve the resolution and determine CNIH3 specific features, unbinned particle images (1.066Å/pixel) were processed (FigS3). The linker between NTD and LBD is flexible and interferes with particle alignment (*1, 2*), and thus focused 3D classification and refinement were conducted in pieces (FigS3-8). In brief, the NTD and the rest of the particle (LBD-TMD-C3) were each classified and refined separately using the respective particle pools that generated the 4.4Å structures of AS and PS. The individual parts were refined to high resolution and molecular models were generated. The resulting maps were rigid body fit into the original 4.4Å maps to reconstruct the full-length architectures. Of note, to refine AS no symmetry was enforced, while C2 was enforced in refining PS. The LBD-TMD-C3 were virtually identical in AS and PS. Thus the LBD-TMD-C3 of AS was re-refined with imposing C2 symmetry, which improved the overall resolution from 3.5Å to 3.3Å. In the reconstructions of LBD-TMD-C3 of AS and PS, at respective overall resolution of 3.3Å and 3.2Å, small portions of CNIH3 remained ill defined. To obtain the best map for the purpose of resolving CNIH3, I combined the particles in the datasets that contributed to LBD-TMD-C3 of AS and PS, imposed C2 symmetry, and calculated the final map of LBD-TMD-C3 with an overall resolution of 3.0Å, the local resolution of the ion channel pore and CNIH3 approaching 2.3Å.

The map LBD-TMD-C3$_{\text{lipid}}$ (FigS9), which was used in Fig 3 and contains high-quality features of the lipid and detergent, was reconstructed from a subset of particles that were classified and refined by enforcing C2 symmetry in all steps of 3D volume image processing, which includes the initial 3D classification of binned images. The rationale for taking the approach is that enforcing C2 should increase the signal-to-noise and enrich particles that contain symmetric features in the combined densities of protein and micelle, which should improve the alignment of lipid/detergent like densities. The overall resolution of LBD-TMD-C3$_{\text{lipid}}$ was 3.3Å, with local resolution of the pore approaching 2.3Å, and the protein portion was nearly identical to the map of LBD-TMD-C3. Further details on the image processing are provided in the methods.

NTD Layer

The NTDs of AS and PS were virtually indistinguishable, and also very similar to the NTD of GluA2$_{\text{cryst}}$ resolved by X-ray crystallography (PDB:3KG2) (*3*) (FigS11A-B). The greater RMSD of the Cα between the NTD of 3KG2 and A2-C3, compared to the RMSD between NTDs of AS and PS, is possibly a result of construct engineering in PDB:3KG2 (i.e. mutating N-glycosylation site at N241 and shortening the NTD-LBD linker, which may restrict the NTD closer to LBD). The native linker may be necessary to accommodate N241 glycosylation, because there is only limited gap available between the NTD and LBD in PDB:3KG2 (FigS11C). The N241 glycosylation may play functional roles in positioning the NTD relative to the LBD, both during gating and spraying apart of NTD layer that occurs upon desensitization (*1*). I note that the glycosylation at N355 and the most peripheral sugars at N241 were only partially resolved in AS, and thus fewer sugars were modeled into the map. I interpret this to be due to the C1 symmetry attenuating the signal-to-noise, because the glycosylation is discernable by lowering the threshold.

The particle images of full-length A2-C3 could not be aligned at high resolution. However, focused classification and refinement of the NTD using the identical pool of raw particle images produced maps of NTD with an overall resolution of 3.1Å in both AS and PS, indicating that the architecture of the NTD tetramer is very well-ordered. Therefore, the NTD layer resembles a rigid body and its position relative to LBD could be determined only at a limited precision. It also implies that the NTD wobbles even in the AS, possibly using the NTD-LBD contact as a pivot point.

Despite the global asymmetry in AS, the NTDs of subunits A and C are related by C2 symmetry. However, a careful inspection revealed a local asymmetry between the NTDs in the neighborhood of K188 (Fig1J). In subunit C, side chain density of K188, which exists at the NTD-LBD contact site, was clearly resolved (FigS11D). However, the corresponding side chain density was absent in subunit A, which does not interact with LBD. This observation implies that the side chain of K188 is engaged and less flexible when the NTD of subunit C makes contact with its own LBD.

What is the functional implication of NTD-LBD contact? The LBD dimer undergoes a conformational change that resembles a closure of the clamshell followed by a rupture of dimer interface during a gating cycle (*4*). The dynamics of LBD could be impacted if NTD is in direct contact. The outcome of such impact may include slowing of activation and/or desensitization. Conversely, motion of the LBD could transmit upwards and influence the stability of the contact made between the two NTD dimers, which is known to dissociate in the desensitized receptors (*1*). These concepts need further experimental evidence to become fully established.

Finally, it is unclear if the AS conformation in the closed channel state is unique to AMPARs associated with CNIH3 or a general property regardless of associated auxiliary subunits. A previous cryo-EM study of intact GluA2 with native NTD-LBD linker have imposed C2 symmetry upfront, and have not fully explored asymmetric architectures from the data pool (*4*).

Asymmetric AMPAR architectures have been reported from native preparations (*1, 5*). Future work using AMPARs with native NTD-LBD linker in conjunction with data processing without imposing symmetry is therefore needed to clarify this issue.

LBD layer and LBD-TMD linkers

The LBD layer is arranged as a dimer-of-dimers. The base of the NTD-LBD linker (V395) is located at the upper part of LBD that interfaces NTD. The V395 is organized nearly identically in A2-C3 and GluA2/stargazin (PDB:5kk2, 5kbu) and GluA2/GSG1L (PDB:5wek) (FigS12B).

The lower part of LBD is attached to the LBD-TMD linkers, which consists of S1-M1, M3-S2, and S2-M4 linkers. The M3-S2 linkers in the BD subunits make the strongest contribution to transducing the ligand induced conformational changes that opens the channel gate (*6-8*). The overall architectures of LBD that face the TMD were very similar to previously reported structures in the closed state, specifically GluA2/stargazin (PDB:5kk2) and GluA2/GSG1L (PDB:5wek). The I633 of LBD directly connects to the M3 gate via M3-S2 linker. The locations of four I633 in the GluA2 tetramer were virtually identical, when A2-C3 was compared with other resting state structures (FigS12B). The M3-S2 linker of A2-C3 also aligned very well (RMSD of Cα = 0.803Å) with a representative resting state structure, GluA2/GSG1L (PDB:5wek) (FigS12C). Overall the LBD and LBD-TMD linker architecture of A2-C3 were consistent with the closed state architectures of AMPAR-auxiliary subunit complexes.

TMD architecture

The compaction of the TMD helices is observed in A2-C3 (FigS13). The M2-filter was unresolved possibly because its architecture accommodates small structural variability. Indeed, earlier structural studies have experienced difficulty resolving this region (*3, 4, 9*). In our structure, the cavity under the M3 bundle is filled with weaker density above noise. I speculate that the critical machinery that controls calcium impermeability in edited R pore is intact even in the presence of a small structural variability. A lipid-like density occludes M2, and thus the M2 polypeptide must be located elsewhere. The M2 may no longer fold as alpha helix to accommodate the filter architecture of the pore within the limited space. The structural reorganization must have a significant impact on gating properties.

It might be possible that the detergents caused the atypical fold of the TMD. However, I believe this is unlikely given that the detergents were used at low concentration, were chemically very mild (i.e. DDM, CHS, GDN, and POPC), and used previously in the cryo-EM studies of AMPARs. Of note, GDN is a synthetic digitonin, a detergent used successfully in the structural studies of AMPAR/TARP and AMPAR/GSG1L complexes that achieved overall resolutions at around 4Å (*6-8*). Further argument is made when I compare the interaction geometry of the TM helices between A2-C3 and AMPAR/γ-8 complex (FigS16B-C). TM2 of CNIH3 and TM4 of γ-8 both interfaces M1. Overall the TM1 of CNIH3 interacts more extensively with M4 than its counterpart TM3 does in γ-8. In fact, TM3(γ-8) is farther away from M4 than TM1(CNIH3) is (FigS16C, arrow). I also observe that the TM2 of CNIH3 pushes the M1 inward towards the central axis of the channel (FigS16B, arrow). From these observations, it is conceivable that binding of CNIH3 induced the atypical TMD architecture. It remains to be seen how compact TMD will impact gating. Future work will address this issue.

Comparing the AMPAR/auxiliary subunit interaction interfaces of A2-C3 and AMPAR/γ-8

The F3, 5, and 8 of CNIH3 make extensive contact with side chains of M1 and M4 of GluA2 at the interface of two proteins (Fig3D-E). The side chain of I177(γ-8) occupies a space that overlaps with F3(CNIH3) (*8*) (FigS16D). F3 interacts with GluA2 at A793(M4) and L789(M4), as well as at Y797(M4) and E524(M1). I177(γ-8) may interact with the same set of residues, except for E524(M1), but at a weaker degree given the smaller size of the side chain. When A793(M4) is mutated to phenylalanine, gating modulations by CNIH3 enhances, whereas gating modulation by stargazin reduces (*10*). Phenylalanine in position 793(M4) would push away both auxiliary subunits from AMPAR. I speculate that such disruption of the interface is favorable for the action of CNIH3 but unfavorable for stargazin. This may imply that the interface of GluA2/CNIH3 undergoes reorganization during gating, whereas stargazin requires stable GluA2/stargazin interface for its action.

The F8(CNIH3) interacts with C528(M1) (Fig3E). The side chain of I173(γ-8) is located near where F8 would be located, however given the different side chain geometry of C528(M1) of GluA2 and its counterpart C524(M1) in GluA1, it is unlikely that I173 interacts with the same residues as F8 (FigS16F). C528 (whose counterpart is C524 in GluA1) is critical for gating modulation in both CNIH3 and γ-8 (*8, 10*). I suggest that the structures of the complex in the gating state and further functional studies would be necessary to explain how C528 (or C524 in GluA1) is utilized in gating modulation by AMPAR auxiliary subunits. Strikingly, there is no side chain of γ-8 occupying the space filled by F5(CNIH3), which interacts with C527 and F531 (FigS16E). In conclusion, the residue contacts were very different in the AMPAR/auxiliary subunit interfaces of A2-C3 and AMPAR/γ-8.

Potential mechanism for gating modulation by CNIH3

The correct topology of CNIH3 and detailed architecture of the interaction interface provides a structural basis to further investigate how signaling through ligand binding is affected by the GluA2-CNIH3 interaction. In the resting state there is no interaction between the LBD and CNIH3. However, this does not exclude the possibility that during gating the dynamic rearrangement of the LBD could reach towards a few amino acids of CNIH3 exposed to the extracellular space. Given that the glutamate sensitivity increases in CNIH3 bound AMPAR (*11*), allosteric coupling between residues of the LBD and CNIH3 must exist. I speculate that the mechanism of CNIH3 action may share some common aspects with the drugs that act through the pre-M1 in NMDA receptors (*12*), because the main binding site of CNIH3 is directly connected to the pre-M1 where lipids were observed (Fig3). Additionally, the global restructuring of the TMD induced by CNIH3 may also impact gating modulation. Structures that represent snapshots of other states will be necessary to understand the mechanism further.

Interpretation of previous mapping of GluA2/CNIH3 interaction

In our previous work, we used peptide arrays to detect interactions between peptide fragments of CNIH3 and purified LBD, and suggested a direct interaction between the LBD and CNIH3 that is in conflict with our cryo-EM structure (*13*). Interaction between peptides synthesized on a cellulose membrane and an isolated domain of a membrane protein may not faithfully reflect the interaction that occurs in the context of an intact complex. The current high-resolution structure of intact GluA2/CNIH3 complex should be regarded as a stronger evidence to describe the interaction interface between the two proteins. All results on the channel gating kinetics obtained from outside out patches co-expressing GluA2 and mutant CNIH3 in (*13*) remain valid.

Materials and Methods

Expression of GluA2/CNIH3 complex:

Rat GluA2 *flip* splice variant with edited (R) pore and mouse CNIH3 cDNA were used. A FLAG epitope tag was placed immediately before the C-terminus of GluA2 (FAT**DYKDDDDK**EGYNVYGIESVKI, where bold case indicates the FLAG epitope), preserving the epitope of the anti-GluA2CT polyclonal antibody. GluA2-FLAG was subcloned into pTREtightVa. A rho1D4 epitope tag was added at the C-terminus of CNIH3 (CMIYTLVSS<u>GGRGG</u>**TETSQVAPA,** where underlined sequence and bold case indicates the linker and 1D4 epitope, respectively). A NotI restriction site was embedded in the amino acid sequence GGR of the linker. The CNIH3-1D4 was subcloned into pTREtightVb between BamHI and EcoRV. The pTREtightVa and Vb were ligated using PacI and AscI sites to produce a plasmid; DualTetONGluA2-FLAG/CNIH3-1D4. The detailed description of pTREtight and dual expression strategy is reported previously (*14*).

Stable cell lines were isolated by co-transfecting plasmids, DualTetONGluA2-FLAG/CNIH3-1D4 and pHyg (a plasmid that confer hygromycine resistance to the host) into HEKTetON cell (CLONTECH), and conducting clonal selection with 120μg/ml hygromycine and 30-60μM NBQX. The clone#7 DOX dependently expresses both GluA2-FLAG and CNIH3-1D4. NBQX was required to keep the cells healthy. Of note, our previously reported cell line clone#3 (*15*) that DOX dependently express GluA2-FLAG (*flip with* R-pore isoform) and constitutively express CNIH3-HA was not suitable for large scale suspension culture, possibly due to the constitutive expression of the CNIH3. The expression of GluA2 and CNIH3, as determined by western blotting, maximized at 28~30 hrs after adding 7.5μg/ml DOX and 1mM sodium butylate. For protein expression, clone#7 was adapted to suspension and grown in Freestyle293 or expi293 media (Thermo Fischer, Life Technologies) with anti-clumping reagent (at 1:500~1000) and 30μM NBQX at 37°C and 6% CO_2. 26~28 hrs after induction, cells were collected by centrifuging at 3000rpm for 10min at 4 °C. After discarding the media, cells were washed with D-PBS once and centrifuged again at 3000rpm for 10 min at 4 °C. After removing the supernatant, the obtained cell pellets were flash frozen in liquid nitrogen and stored at -80 °C. The expi293 media typically produced 15ml of cell pellet per 1L of culture, whereas with the Freestyle media the yield was 5ml. The expression of GluA2 and CNIH3 was higher in the Freestyle media than in expi293.

Purification of GluA2-CNIH3 complex:

The following purification was conducted at 4 °C. 20ml of frozen cell pellet was resuspended in buffer containing 20mM TrisHCl pH8.0, 150 mM NaCl, 2mM TCEP, 30μM NBQX, and protease inhibitors (1mM PMSF, 10μg/ml leupeptin, 10μg/ml aprotinin, 0.5mM benzamidine, 1 μg/ml pepstatinA). Total volume after resuspending was 180ml. 20ml of 10x detergent (3%DDM, 0.6% cholesterol hemi succinate, 60mM TrisHCl pH8.0, 150 NaCl, 1mg/ml POPC) was added and the mixture was rocked gently for 3hrs. The lysate was centrifuged at 3000rpm for 10 min to remove large debris and further ultracentrifuged at 45,000rpm in 45Ti rotor (Beckman) for 1hr. The supernatant was incubated in batch with 2ml of FLAGM2 agarose beads (Sigma) for 3 hr. The beads were collected by centrifugation at 500rpm for 5min and transferred into an empty column. The beads were washed for 6 column volumes with wash buffer (0.05% GDN, 20mM TrisHCl pH8.0, 150mM NaCl). The proteins were eluted using wash buffer containing 0.5mg/ml FLAG peptide. The first elution fraction was 1.8 ml. In the second elution, 10.2 ml of elution buffer was passed through the column and the eluate was collected. The second elution fraction was concentrated down to 0.55ml using Ultrafree 100KDa MWKO ultrafiltration. The concentrated sample was ultracentrifuged at 35,000 rpm for 15 min and applied to Superdex200 Increase column (GE Healthcare) equilibrated with GF buffer (0.05% GDN, 20mM TrisHCl pH8.0, 150 mM NaCl). The isocratic elution (0.5ml per fraction) was conducted at flow rate 0.5 ml/min. The peak fractions (typically two fractions, frac8 and 9) were combined and concentrated down to 50µl using Ultrafree 100KDa MWKO ultrafiltration.

Specimen preparation, pre-screening of grids, and cryo-EM imaging:
Purified protein was immediately used to make vitrified specimen. The time required from dissolving the membrane to completing grid preparation was kept within 12~14hrs. Protein solution was mixed with antagonist ZK200775 at final concentration of 280µM for 30 min prior to freezing. 2µl of protein (5mg/ml) was applied to a glow discharged (25mA 30sec, Quorum Emitech K100X) Quantifoil 1.2/1.3. Vitrified specimen was obtained by plunging grids into liquid ethane using Vitrobot MK4 (Thermo Fisher) under the following plunging condition; temperature 4^{o}C, humidity 100%, wait time 30sec, blot force 10, blot time 2.5 sec, and drain time 0sec. The optimal conditions were screened and identified using the FEI TF20 microscope.

Further pre-screening was conducted in FEI Polara microscope operated at 300keV and equipped with Gatan K2 Summit Direct Electron Detector. 1311 micrographs were collected at low dose condition (total exposure 53e$^-$/Å^2 over 50 frames, exposure time 12sec) using SerialEM at a nominal magnification of 31,000X, which corresponds to 1.247 Å/pixel at image level. The imaging defocus range was -0.8 to -2.0µm at 0.1µm increments. Two grids that were frozen at the same time as the one that was confirmed to produce the 5.6Å structure from the Polara dataset (focused classification and refinement of LBD, TMD, CNIH3 using 15,574 particles in the final reconstruction) were imaged using Titan Krios.

Cryo-EM grids were transported using a dry-shipper from Vanderbilt to University of Tokyo. Micrographs were recorded using the Gatan Bioquantum K3 summit direct electron detector mounted on a Titan Krios (Thermo Fisher). Images were taken at nominal magnification of 81K, which corresponds to 1.066Å/pixel in the image. Serial EM was used for automated image collection using image shift to shoot nine holes per one focus point in low dose mode. The exposure was 0.12 sec/frame over 6 sec at 11.551e$^-$/pixel/sec, a total exposure of 58.548e$^-$/Å^2. The imaging defocus range was -0.8 to -2.0µm at 0.12µm increments.

Image processing of dataset of GluA2-CNIH3 complex collected on Titan Krios:
The overview of image processing is described as a chart in FigS3. FigS4-9 are referenced from FigS3.

Initial processing (FigS4)
All processing was done using RELION3 (*16*). Each raw movie stack containing 50 frames was motion corrected (at 4x4 patches) and dose weighted (1.171e$^-$/Å^2/frame) using Motioncorr2 (*17*). Dataset consisting of 11,340 micrographs was split into four batches of similar sizes (in micrograph numbers; batch1=1-2286, batch2=2,287-5,302, batch3=5,303-8,163, and

batch4=8164-11,340) and processed separately at the beginning to optimize the computational cost. The following procedures were undertaken for each batch unless otherwise specified.

CTF was estimated using CTFFIND4 (*18*) using patches of 1024x1024 pixels. The rlnCTFMaxResolution formed unimodal histogram with mode=3Å with the majority of the values between Nyquist (2.132Å) and 5Å. Micrographs with rlnCTFMaxResolution ≤ 6Å were used for further processing. About 2000 particles were manually picked from two hundred micrographs and were subject to 2D classification into 8 classes. Six class averages that contained representative features of AMPARs were selected and used as templates for AutoPick. From four batches, 1.47 x10^6, 1.86 x10^6, 1.63 x10^6, and 1.91 x10^6 particles were picked, respectively, totaling 6.87 x10^6 particles.

Particles were extracted at a box size of 350x350 pixels and rescaled to 64x64 pixels. After 2D classification into 200 classes, particles that generated class averages with well-defined features of AMPARs were selected. Selected particles were re-extracted at a box size of 360x360 pixels with re-centering and rescaled to 180x180 pixels (i.e. equivalent to binning by a factor of 2). A second round of 2D classification into 100 classes was conducted. Particles that generated class averages containing well-defined secondary structure features were selected from each batch. Good averages from all batches were combined (~920,000 particles) to proceed to 3D classification. A cryo-EM density map of GluA2 tetramer bound to ZK200775 (EMD-2680) was used as reference for 3D classification into 4 classes without imposing symmetry (i.e. C1 symmetry). Two classes, Class1 and Class3, produced maps that exhibited well-defined features of AMPAR with large detergent micelle. The 3D auto-refinement followed by post processing generated maps at an overall resolution of 4.41Å, while the Nyquist limit of the binned dataset is at 4.264Å. These maps, derived from Class1 and Class3, will be referred to as A2-C3(AS) and A2-C3(PS), respectively.

Focused classification and refinement of NTDs (FigS5 and 6)

Particles contributing to A2-C3(AS) and A2-C3(PS) were re-extracted at a box size of 360x360pixels without binning. In each conformation, 3D classification specifying 3 classes was initiated using the full-length for 20-30 iterations. C1 and C2 symmetry were imposed for AS and PS, respectively. Then 3D classification was continued by imposing a local search, with a mask that covers the NTDs and setting regularization parameter at 20, for another 40 iterations. Output of focused classification of AS produced one high quality class that showed polypeptide backbones and side chain bumps at a wide range of threshold. PS produced two high-quality classes with identical shapes, and thus the two classes were combined. Refine3D were both conducted with the NTD masks and local search turned on, imposing the same symmetry used during classification. PostProcess produced maps of overall resolution 3.1Å (masked, FSC=0.143) for each conformation. These maps were used to build atomic models. Local resolution was calculated using ResMap and Relion3.

Focused classification and refinement of LBD-TMD-C3(AS) and LBD-TMD-C3(PS) (FigS7)

Particles contributing to A2-C3(AS) and A2-C3(PS) were re-extracted at a box size of 360x360pixels without binning, but with re-centering by setting the new origin to coordinate (0,0,-20) so that the gate of the AMPAR will be the new center. The particles were subject to focused 3D classification specifying 3 classes by imposing a local search and a mask that excludes both the NTDs and detergent micelle. No symmetry was imposed for both AS and PS. In AS, class2 containing 84,584 particles produced a well-defined structure with polypeptide backbone and bumps of side chains. The particles in this class were subject to Refine3D in two steps. The rationale is to evaluate the architecture of the C1 and examine if there is any asymmetric feature between subunits A and C at the junction of NTD-LBD contact site. The 3.51Å map produced with C1 symmetry, after Refine3D and PostProcess, showed no evidence for asymmetry in the LBD-TMD-C3(AS) architecture. Therefore, C2 symmetry was imposed to conduct Refine3D and PostProcess, which produced a map of overall resolution at 3.28Å (masked, FSC=0.143). In PS, class1 containing 76,689 particles produced a well-defined map. The particles were subject to Refine3D and PostProcess with the same mask, and with C2 imposed. The output, LBD-TMD-C3(PS), was a map of overall resolution at 3.22Å (masked, FSC=0.143). Local resolution was calculated using ResMap and Relion3. In Fig1B, the map of LBD-TMD-C3(AS) obtained without imposing symmetry is displayed.

Focused classification and refinement of LBD-TMD-C3 (FigS8)

Inspection of LBD-TMD-C3(AS) and LBD-TMD-C3(PS) indicated that the two structures were virtually identical. After generating atomic models, the two models aligned with RMSD of Cα = 0.526Å. I also realized that small portions of CNIH3 densities were ill-defined in the individual map of LBD-TMD-C3(AS) and LBD-TMD-C3(PS). For the purpose of revealing high quality map of CNIH3, as well as LBD-TMD-C3, I combined the particles in AS and PS. Then, first round of Refine3D and PostProcess were conducted with C2 imposed to generate a map of LBD-TMD-C3 with overall resolution at 3.12Å (masked, FSC=0.143). Further CTF refinement, astigmatism refinement, and beam tilt refinement followed by a second round of Refine3D and PostProcess improved the overall resolution to 2.97Å (masked, FSC=0.143). This map was used to generate an atomic model. Local resolution was calculated using ResMap and Relion3.

Focused classification and refinement of LBD-TMD-C3$_{lipid}$ (FigS9)

The lipid/detergent-like densities were observed in all of the high-resolution LBD-TMD-C3 maps, however, at different qualities, which were primarily due to differences in signal-to-noise. The lipids were best resolved in the map LBD-TMD-C3$_{\text{lipid}}$ that was reconstructed from a subset of particles that were classified and refined by enforcing C2 symmetry in all steps of 3D volume image processing. I interpret the approach was effective because enforcing C2 should (1) improve signal to noise and (2) select those particles with homogeneous relative geometry between the AMPAR and the micelle, and improve the alignment of lipid/detergent like densities associated with the receptor. In precise, the initial 3D classification of binned images was conducted specifying 4 classes. Particles in class2, whose map contains well-defined features of polypeptides at a wide range of threshold, were selected and re-extracted as unbinned images. Subsequent Refine3D and PostProcess produced a map of an overall resolution of 3.28Å. CTF refinement, beam tilt refinement, 2nd round of Refine3D, and PostProcess were conducted. The resolution did not improve by the additional refinement, but the appearances of the lipid/detergent-like densities were improved. The number of particles that contributed to the final map is smaller than those that contributed to LBD-TMD-C3 but greater than LBD-TMD-C3(AS) or LBD-TMD-C3(PS), indicating that strictly enforcing C2 has selected a subset of particles with well-ordered lipids and improved signal over noise. The protein portion of LBD-TMD-$C3_{lipid}$ was virtually identical to LBD-TMD-C3, despite the difference in resolution (3.28Å vs. 2.97Å). A local resolution was determined using ResMap and Relion3. The map LBD-TMD-$C3_{lipid}$ is used in Fig3.

Model building and validation:

Atomic models of NTD(AS) and NTD(PS) were built using the NTD of PDB 3KG2 as a reference. The model was positioned manually into the EM density map and further adjusted using the jiggle fit function in Coot (*19*). Further manual adjustment with real space refine zone function in Coot was used to generate an atomic model.

Atomic models of LBD and TMD of GluA2 were built using the atomic model of GluA2 in complex with stargazin (PDB 5kk2) as a reference. First, stargazin and NTD of GluA2 were removed from the 5kk2 to generate a model of the LBD and TMD. The model was positioned manually into the EM density map and further adjusted using the jiggle fit function in Coot (*19*). The LBD portion of the model was oriented correctly into the map but the TMD was deviating. The models of the TMD helices were detached from the LBD and each helix was manually placed into the map. Further manual adjustment with real space refine zone function in Coot was used to generate an atomic model for the LBD and TMD of GluA2.

Atomic model of CNIH3 was built *de novo* using coot (*19*). Algorithms of Jpred4 (*20*) predicted that CINH3 has 3 TM helices, where TM1, 2, and 3 have 33, 44, and 33 amino acids, respectively. However the map clearly had four TM helices. Each helix contained at least one tryptophan and many aromatic residues in unique order such that the amino acid sequence was unambiguously modeled into the density map. The model revealed that the TM2 folds onto itself lack a jack knife and spans the membrane twice. The amino and carboxyl terminal both exist in the extracellular space. Contrary to previous literature that models CNIH3 as a protein that spans the membrane three times, our data and model is consistent with spanning the membrane four times. The densities of the cytoplasmic linkers were ill-defined and were not modeled.

The generated model was further refined using the real_space_refine tool in Phenix (*21*). Real space refinement was conducted by imposing secondary structure restrains by annotating helices and sheets in the PBD file. To prevent overfitting of the models into the density, refinement was run for five cycles with strict geometric restraints of 0.005-0.01 for bond length and 0.5-1 for bond angle while non-crystallographic symmetry (NCS) consistent with C2 symmetry of the map was imposed when necessary. FCS of model vs map was output by Mtriage. Cryo-EM validation tools MolProbity and Mtriage were used for validation (summarized in TableS1). The FSC_{work} vs FSC_{free} were calculated as described (*22*). In brief, first, phenix.dynamics was run to scramble the atoms in the model by rmsd 0.5Å. The shaken model was refined against the half1-map to obtain FSC_{work}, which was the FSC calculated between refined model vs half1-map. Next, FSC_{free} was calculated between the refined model (i.e. the model calculated by refining the shaken model against the half1-map) and half2-map. PyMol and Chimera were used to display and analyze results.

Electrophysiology

The stable cell lines derived from TetON HEK cells were plated on coverglass coated with poly-D-lysine (37.5 µg/ml in H_2O) for 15 min. Excess coating material was removed by washing in D-PBS three times. Cells were plated and incubated on coverglass until they were adherent (typically within 12hrs) and then 30µM NBQX and 5µg/ml doxycycline (DOX) was added. Cells were used for recording 24-36 hr after induction. Ligand (1mM glutamate) was applied via theta tubing glass capillary mounted on a piezo actuator (P-830.30, Physik Instrumente) controlled by an LVPZT amplifier (E-505, Physik Instrumente), DAQ device (NI USB-6221, National Instruments), and LabView software (National Instruments). Recording was done using a single channel of a Multiclamp700B Amplifier (Axon Instruments) operated by pClamp10 software. Signals were digitized using Digidata1440A (Axon Instruments) at a sampling rate of 50 kHz and low pass filtered at 2kHz. Borosilicate glass capillaries (O.D. 1.5 mm, I.D. 0.86 mm, Sutter) were pulled to manufacture electrodes with pipette resistances of 3.5-5 MΩ. Internal solution was (in mM) 110 NaCl, 10 NaF, 5 EGTA, 0.5 $CaCl_2$, 1 $MgCl_2$, 10 Na_2ATP, 5 HEPES, adjusted to pH7.3 with CsOH and 295 mOsm. External solution was (in mM) 145 NaCl, 2.5 KCl, 1.8 $CaCl_2$, 1 $MgCl_2$, 5 HEPES, 10 glucose, adjusted to pH7.3 with NaOH and 301 mOsm. Standard solution without ligand was the external solution. The ligand solution contained 1mM glutamate in external solution, supplemented with 2mM glucose and 3mM NaCl to facilitate visualizing the interface of the two solutions and recording liquid junction potential after breaking the patch. The 20-80% rise time of liquid junction potential, measured after breaking the patch, was ~300µs. Decay of AMPAR mediated current was fit to single and double exponential decay (using pClamp10) for currents recorded in the presence of CNIH3 and GSG1L, respectively. Weighted decay time constant ($\tau_{w,des}$) was calculated as previously reported(*23*).

Cysteine crosslinking nearby residues in A2-C3

Disulfide bond may form between residues, whose Cα are separated by approximately 5.5 to 7.5Å. Pairs of residues at the interface that meet the condition were identified, as shown in the table in FigS18A, and mutated to cysteine using *in vitro* mutagenesis as described (*10*). The starting material cDNA for FLAG tagged GluA2 and 1D4 tagged CNIH3 were identical to those described above. The variants of GluA2 and CNIH3 were subcloned into pTREtVa and pTREtVb (*14*), respectively. The pTREtVa-GluA2(wt or mutant) and pTREtVb-CNIH3(wt or mutant) were combined as described (*14*) to generate a DualTetON expression plasmids that each co-express a variant of GluA2 and a variant of CNIH3 in a DOX inducible manner. Each plasmid was transfected into TetONHEK cells plated in a 10cm dish using calcium phosphate method. The cells were induced with 10µg/ml DOX in the presence of 45µM NBQX for 24 hours. The transfected cells were pipetted off the dish and centrifuged at 500 rpm for 5 min. The media was discarded and the cells were washed with ice cold D-PBD containing 30µM NBQX once and flash frozen in liquid nitrogen and stored at -80C^o.

The following biochemical procedure was conducted at 4C^o.The frozen cells were resuspended in a buffer containing 20mM TrisHCl pH8.0, 150 mM NaCl, 30µM NBQX, and protease inhibitors (1mM PMSF, 10µg/ml leupeptin, 10µg/ml aprotinin, 0.5mM benzamidine, 1 µg/ml pepstatinA). Total volume after resuspending was 900µl. 100µl of 10x detergent (3%DDM, 0.6% cholesterol hemi succinate, 60mM TrisHCl pH8.0, 150 NaCl, 1mg/ml POPC) was added and the mixture was rocked gently for 1.8hrs. The lysate was centrifuged at 15000rpm for 10 min. The supernatant was incubated for 1hr at 4C^o with 50µl of FLAGM2 agarose beads (Sigma), which were pre-equilibrated with the same detergent-containing buffer used for cell lysis. The beads were washed twice with 1ml of buffer containing 0.3%DDM, 0.06% cholesterol hemi succinate, 0.1mg/ml POPC, 26mM TrisHCl pH8.0, 150 mM NaCl, 30µM NBQX, and protease inhibitors (1mM PMSF, 10µg/ml leupeptin, 10µg/ml aprotinin, 0.5mM benzamidine, 1 µg/ml pepstatinA). The GluA2/CNIH3 complexes were eluted by adding to the beads 150µl of wash buffer supplemented with 0.5mg/ml FLAG peptide. The beads were incubated for 10min, during which it was gently resuspended. The beads were spun down and the supernatant was recovered. Each sample was split into two fresh 1.5ml tube; one tube was mixed with SDS-PAGE sample buffer that contains 100mM DTT, the other without DTT. The tubes were incubated at 50 C^o for 15 min and then at room temperature for 15min. 6% gel SDS-PAGE was conducted to separate high molecular range GluA2 and crosslinked GluA2-CNIH3, while 12.5% gels were used to separate free CNIH3. Western blots were conducted using anti-GluA2CT (polyclonal and described in (*24*)) and anti-1D4 (monoclonal, Cube biotech) antibodies.

Supplementary Figures

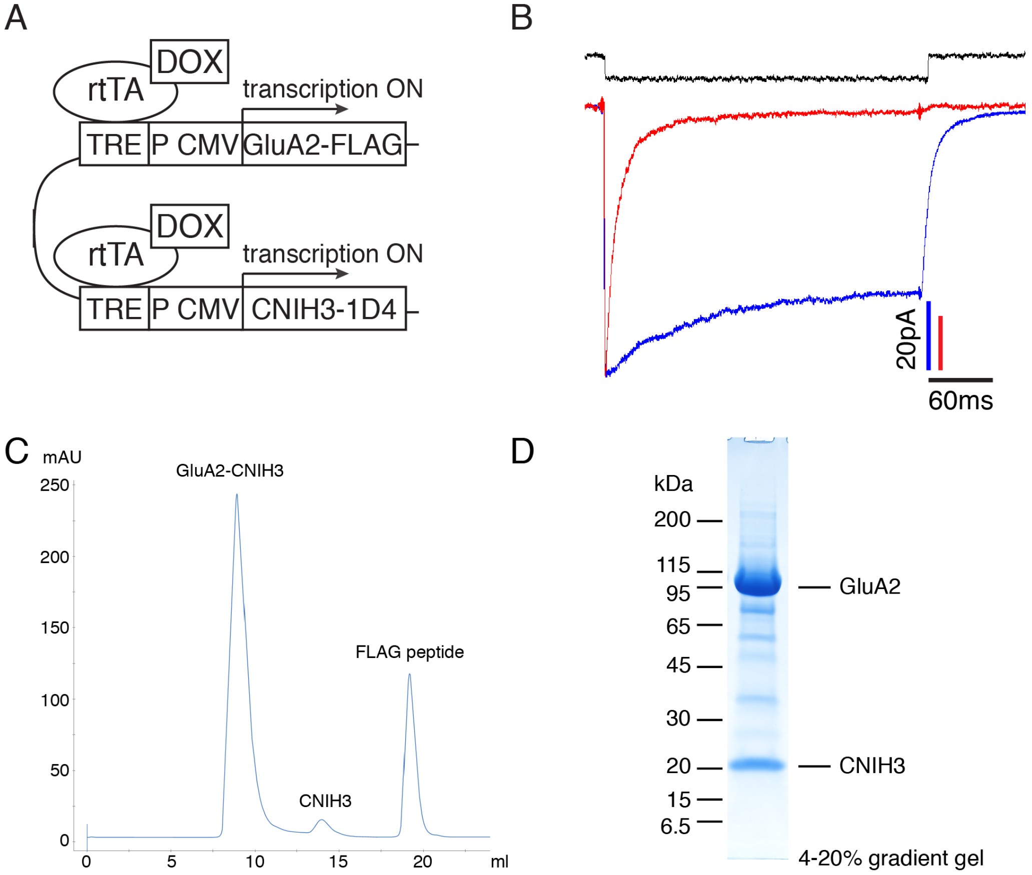

Figure S1. Functional characterization, expression, and purification of GluA2-CNIH3 complex.

(A) GluA2 and CNIH3 were stably co-expressed, independently without tether, in a DOX dependent manner from a HEK cell line.

(B) Glutamate induced currents from the GluA2/CNIH3 expressing cell line exhibit slow desensitization. Representative current trace recorded from an outside out patch is shown. Top black trace: Open tip response after breaking the patch. Red trace: GluA2iR/GSG1L, Blue trace: GluA2iR/CNIH3. Red and blue traces are peak normalized. The GluA2iR/GSG1L was also expressed in the context of a stably expressing HEK cell line using a dual DOX dependent expression, such as shown in A. The expressed GluA2/CNIH3 (t=75.2±5.02 ms, n=6) and GluA2/GSG1L complexes demonstrated slow desensitization (fast decay component t_{fast}=9.37±0.37 ms, slow decay component t_{slow} = 50.8±10.8 ms, weighted decay constant $t_{w,des}$ = 15.5±0.54 ms, n=8, where ±SEM is provided) when ion channel current was recorded from outside-out patches obtained from these cell lines, confirming that the complex is functional. A 300ms pulse of 1mM glutamate was applied to the patch via theta tubing controlled by a piezo actuator in a fast-ligand application system, where the 20-80% rise time of liquid junction potential, measured after breaking the patch, was ~300µs.

(C) Superdex200 gel filtration chromatography at the final step of purification.

(D) 4-20% SDS-PAGE gel of the peak fraction shown in C.

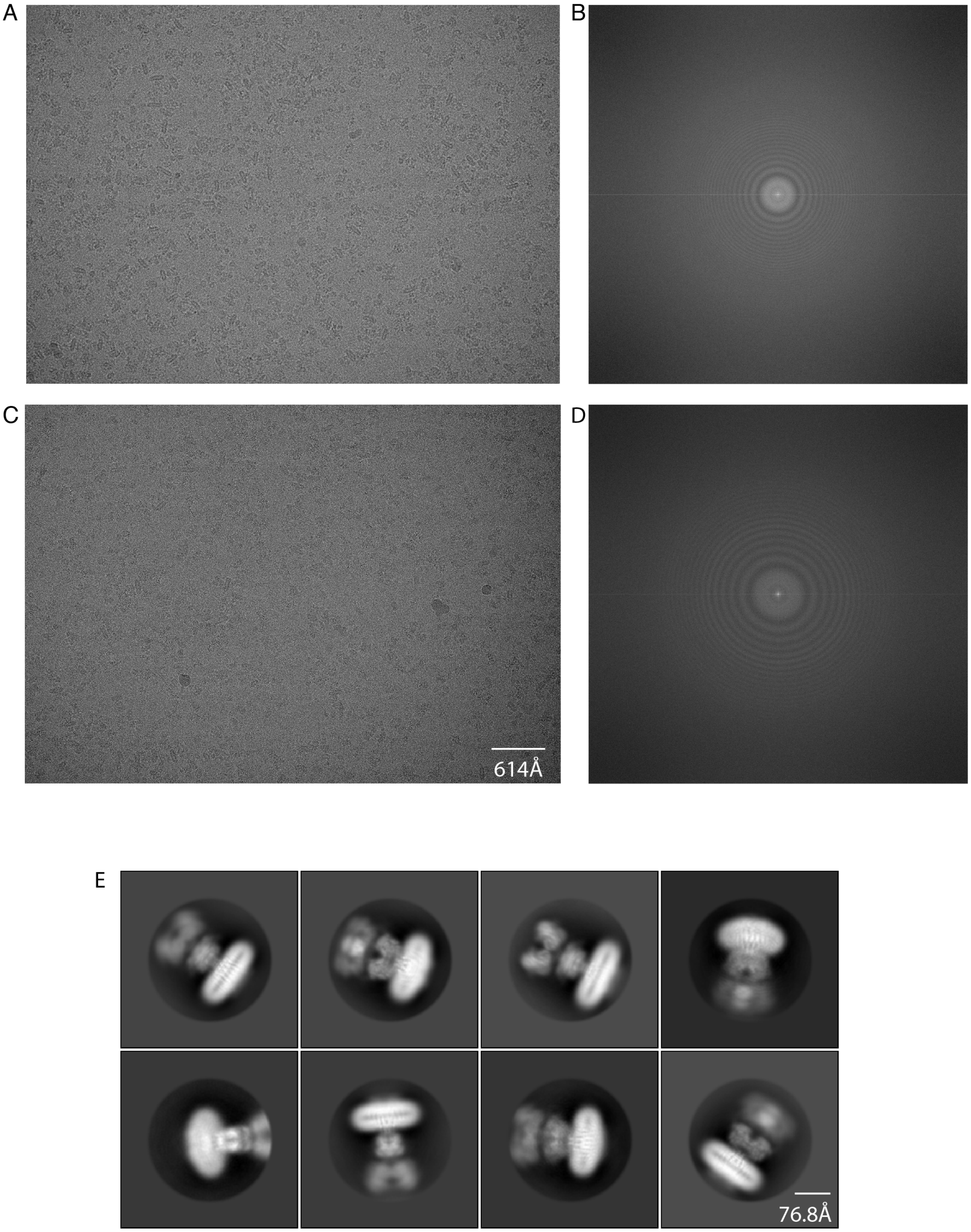

Figure S2. Representative micrographs of GluA2-CNIH3 complexes recorded on GatanK3 summit direct electron detector.
(A and C) Representative motion corrected micrographs recorded on Gatan BioQuantum K3 detector. Defocus = -1.9µm (A) and -0.96µm (C).
(B and D) Fourier transforms of images in (A) and (C).
(E) Representative 2D class averages of GluA2-CNIH3 complexes

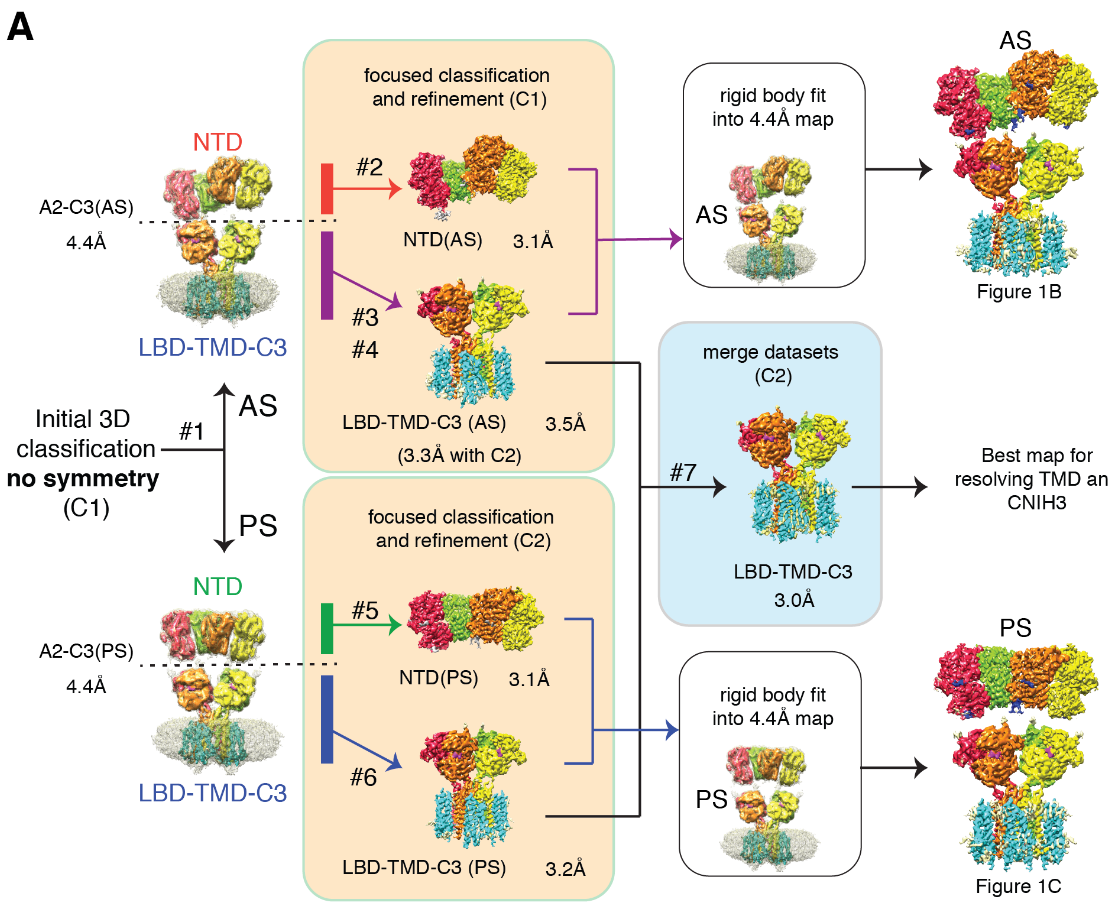

#1. Derivation of 4.4Å maps of full length AS and PS: FigS4

#2. Derivation of 3.1Å map of NTD(AS) with C1 symmetry enforced: FigS5

#3. Derivation of 3.5Å map of LBD-TMD-C3(AS) with C1 symmetry enforced: FigS7

#4. Derivation of 3.3Å map of LBD-TMD-C3(AS) with C2 symmetry enforced: FigS7

#5. Derivation of 3.1Å map of NTD(PS) with C2 symmetry enforced: FigS6

#6. Derivation of 3.2Å map of LBD-TMD-C3(PS) with C2 symmetry enforced: FigS7

#7. Derivation of 3.0Å map of LBD-TMD-C3 with C2 symmetry enforced: FigS8

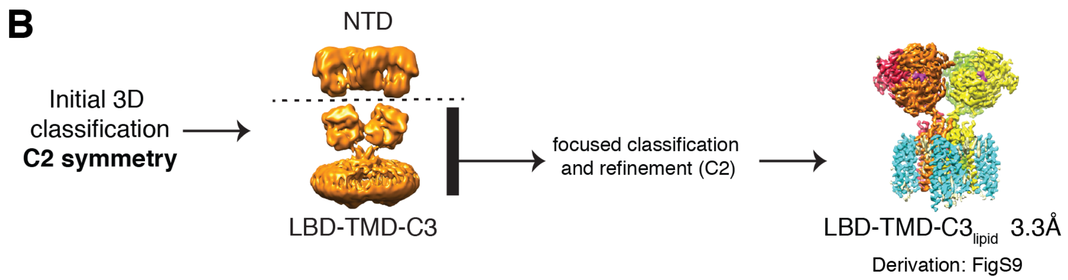

Figure S3 Image processing workflow of dataset collected by Titan Krios.
The charts (**A** and **B**) in the current figure are described in detail in the methods. Workflow **B** was necessary to resolve lipid/detergent like density and displayed separately. The derivation, characterization, and validation of each map are described in detail in FigS4-9, as listed above.

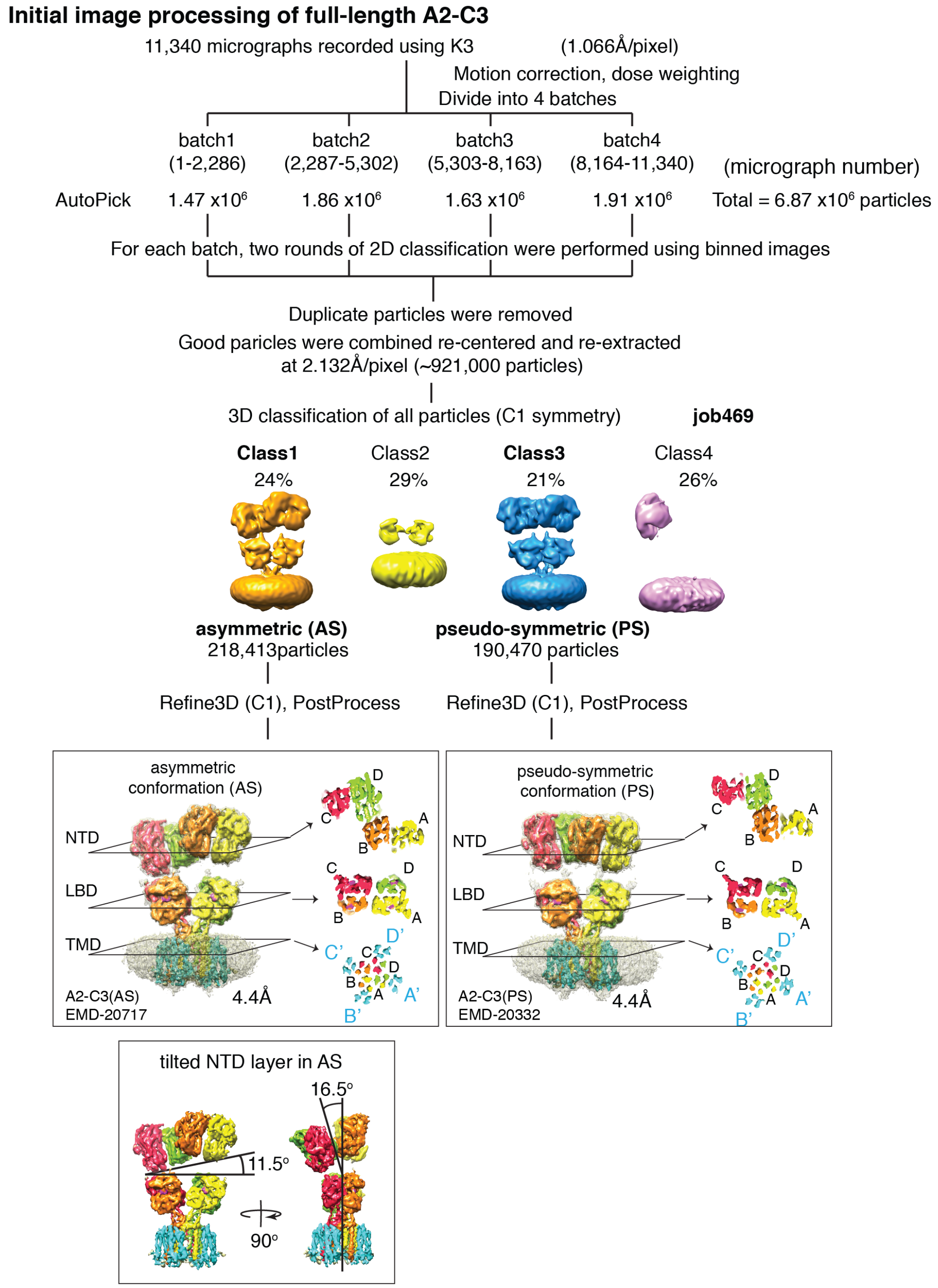

Figure S4. Image processing of full-length A2-C3 without imposing symmetry
Approximately 921,000 particles were selected from 2D classification. To detect both symmetric and asymmetric conformations, no symmetry was imposed during 3D classification. Class1 (gold) and class3 (blue) each produced well-defined map, and were subject to refinement and post-processing, without imposing symmetry. Maps of AS and PS, each with an overall resolution of 4.4Å, were produced. The AS and PS are each shown by superimposing its map at two different thresholds, to visualize the complex with or without micelle. The four subunits in

AS and PS are labeled A (yellow), B (orange), C (red), and D (green). The cross sections at the level of NTD, LBD, and TMD are shown. Cyan densities are CNIH3, labeled as A’-D’. For clarity, the degree of asymmetry of the NTD layer in AS is characterized without the micelle from two views in a separate box on the left bottom.

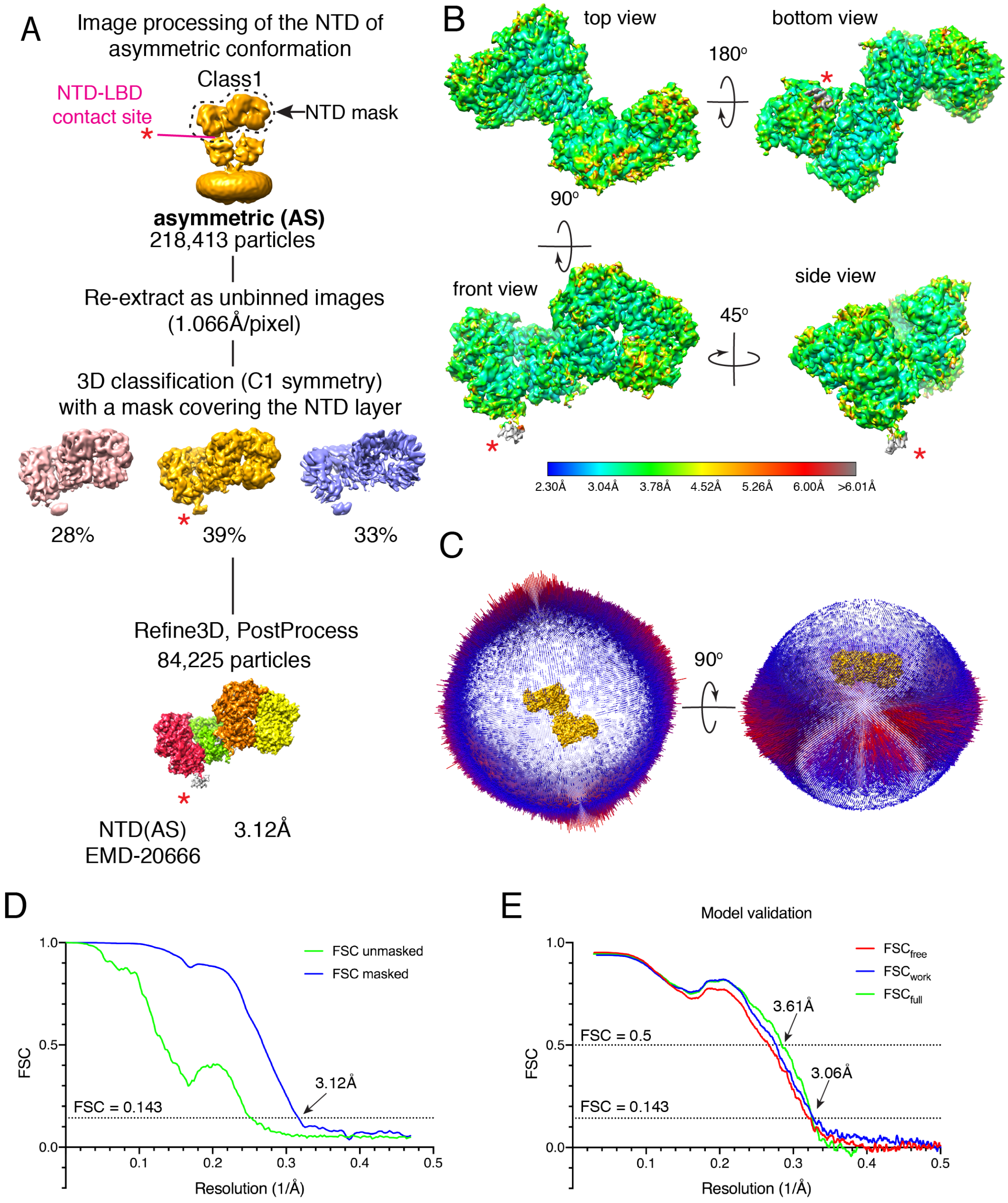

Figure S5. Angular distribution, local resolution, FSC curves, and model validation of the NTD(AS).

(A) Image processing workflow. The map was derived from focused classification and refinement of the NTD of AS (Class1 from FigS4), using a mask limited to the NTD layer. No symmetry was imposed. The asterisk in magenta indicates the junction with LBD, which is contained in the mask.

(B) Local resolution was calculated using ResMap. The color map indicates the resolution, which ranges between 2.3 to 6.0Å, the majority of the density is between 3.0 and 3.5Å. The red asterisk indicates the junction with LBD.
(C) Distribution of the assigned angles of the particles that contributed to the final reconstruction. Excellent sampling of views for reconstruction is demonstrated.
(D) Fourier shell correlation (FSC) derived from half maps. FSC from masked maps and unmasked maps are shown. The position that corresponds to FSC=0.143 is indicated by a dotted line. Intersections of the FSC plots and FSC=0.143 is highlighted by an arrow together with the resolution estimates.
(E) Validation of the model vs map. FSC_{full} indicates FSC of the model against the full map. The difference between FSC_{work} and FSC_{free} was small, indicating minimal overfitting.

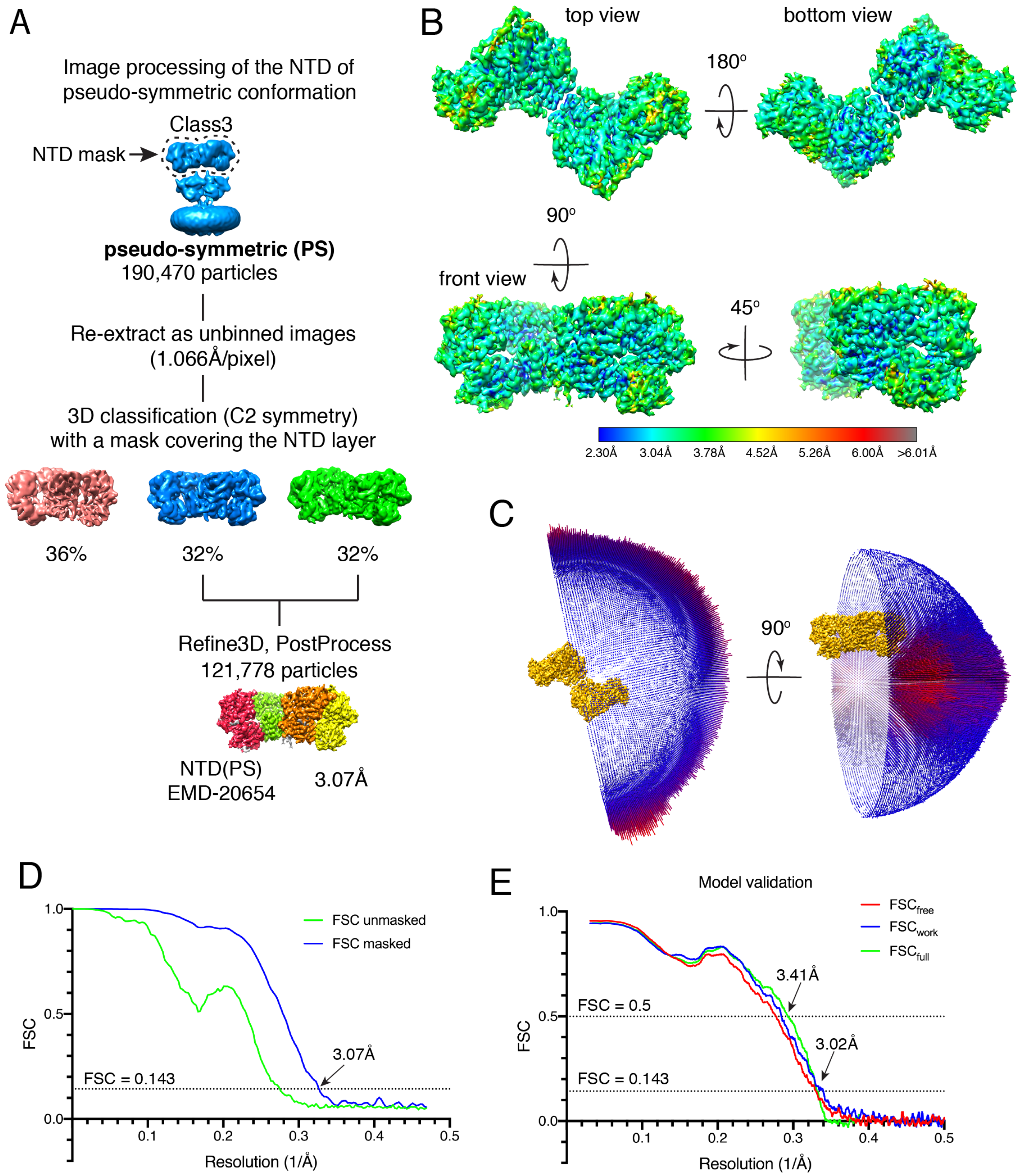

Figure S6. Angular distribution, local resolution, FSC curves, and model validation of the NTD(PS).

(A) Image processing workflow. The map was derived from focused classification and refinement of the NTD of PS (Class3 from FigS4), using a mask limited to the NTD layer. C2 symmetry was imposed.

(B) Local resolution was calculated using ResMap. The color map indicates the resolution, which ranges between 2.3 to 6.0Å, the majority of the density is between 2.3 and 3.5Å.

(C) Distribution of the assigned angles of the particles that contributed to the final reconstruction. Excellent sampling of views for reconstruction is demonstrated.
(D) Fourier shell correlation (FSC) derived from half maps. FSC from masked maps and unmasked maps are shown. The position that corresponds to FSC=0.143 is indicated by a dotted line. Intersections of the FSC plots and FSC=0.143 is highlighted by an arrow together with the resolution estimates.
(E) Validation of the model vs map. FSC_{full} indicates FSC of the model against the full map. The difference between FSC_{work} and FSC_{free} was small, indicating minimal over fitting.

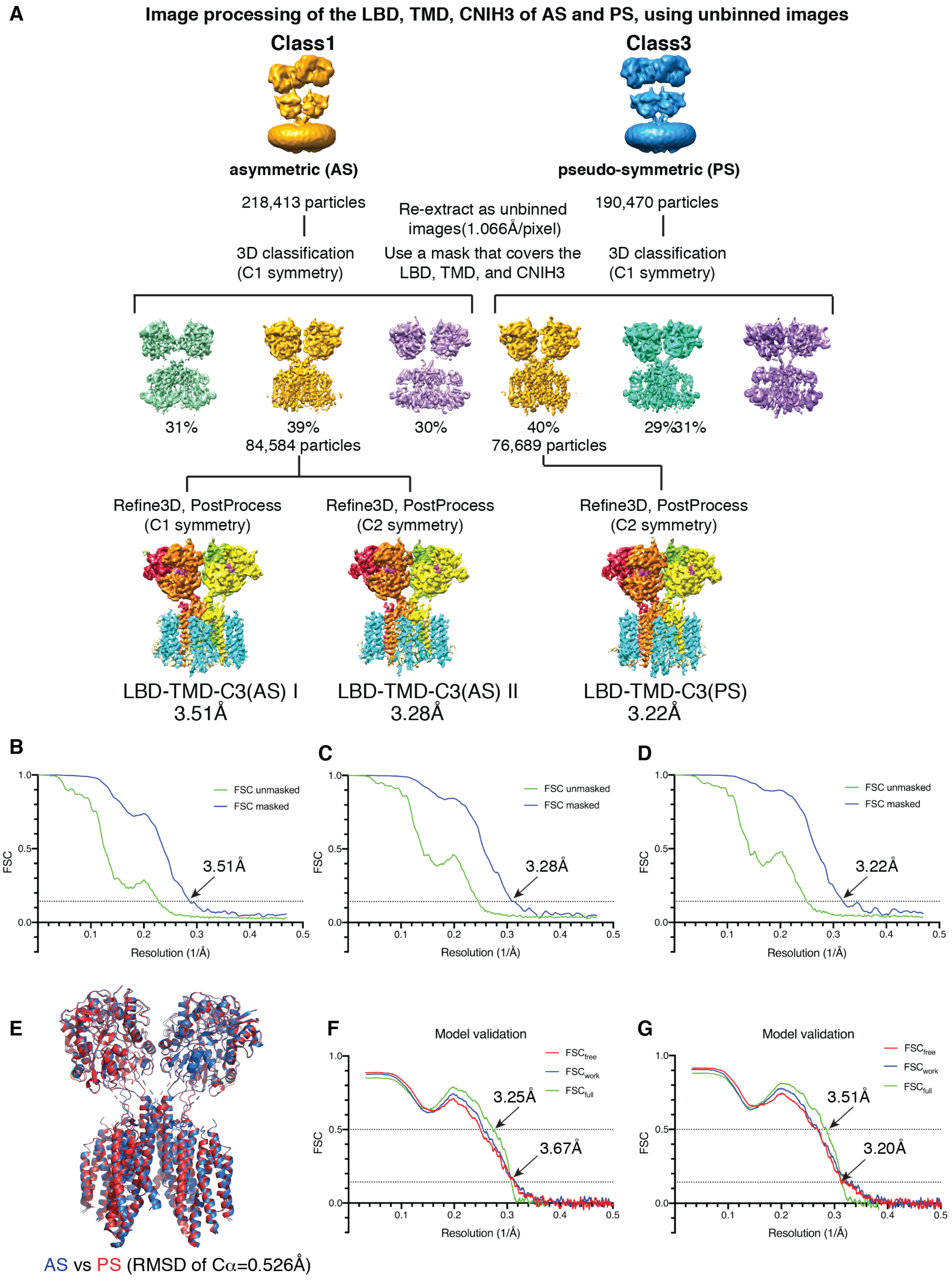

Figure S7. Image processing, FSC curves, and model validation of the LBD-TMD-C3(AS) and LBD-TMD-C3(PS).

(A) Image processing workflow. The final maps were derived from focused classification and refinement of the AS (Class1 from FigS4) and PS (Class3 from FigS4), using a mask excluding

the NTD layer and detergent micelle. The symmetry used in each step is indicated. Inspection of LBD-TMD-C3(AS) I, which was calculated with C1, confirmed that it is C2 symmetry. Therefore LBD-TMD-C3(AS) II, which was calculated by C2, was used for further analysis.
(B-D) Fourier shell correlation (FSC) derived from half maps is shown for each reconstruction. B=LBD-TMD-C3(AS) I, C=LBD-TMD-C3(AS) II, and D= LBD-TMD-C3(PS). FSC from masked maps and unmasked maps are shown. The position that corresponds to FSC=0.143 is indicated by a dotted line. Intersections of the FSC plots and FSC=0.143 is highlighted by an arrow together with the resolution estimates.
(E) Alignment of models of LBD-TMD-C3(AS) II and LBD-TMD-C3(PS). Two models were virtually identical (RMSD of Cα=0.526Å).
(F-G) Validation of the model vs map. F=LBD-TMD-C3(AS) II and G= LBD-TMD-C3(PS). FSC_{full} indicates FSC of the model against the full map. The difference between FSC_{work} and FSC_{free} is insignificant, indicating minimal over fitting.

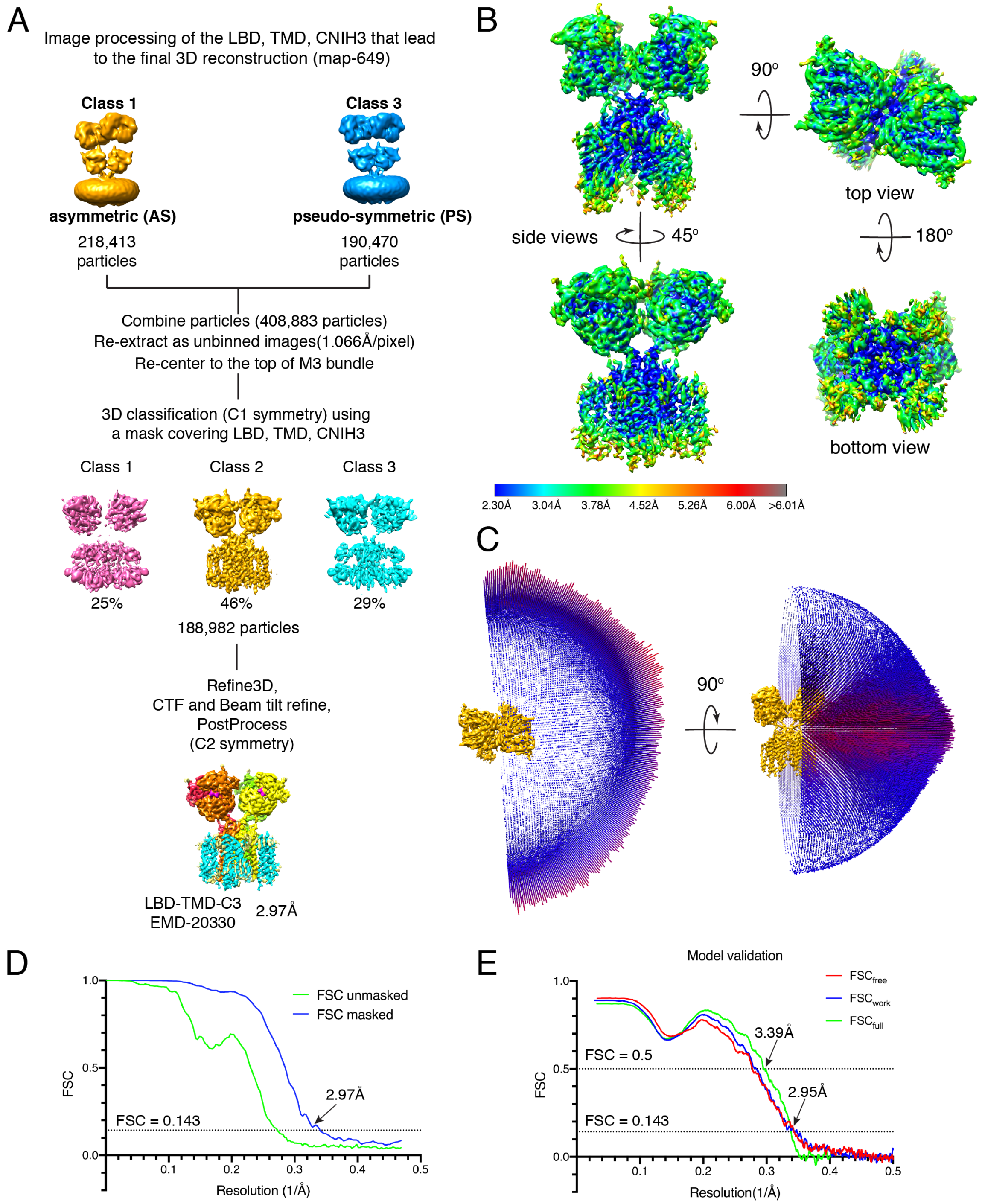

Figure S8. Angular distribution, local resolution, FSC curves, and model validation of the LBD-TMD-C3.

(A) Image processing workflow. The map was derived from focused classification and refinement of the LBD-TMD-C3 using particles from both AS and PS (Class 1 and 3 from FigS4). A mask excluding the NTD layer was applied. C2 symmetry was imposed at refinement and post-processing.

(B) Local resolution was calculated using ResMap. The color map indicates the resolution, which ranges between 2.3 to 6.0Å, the majority of the density is between 2.3 and 3.5Å.

(C) Distribution of the assigned angles of the particles that contributed to the final reconstruction. Excellent sampling of views for reconstruction is demonstrated.
(D) Fourier shell correlation (FSC) derived from half maps. FSC from masked maps and unmasked maps are shown. The position that corresponds to FSC=0.143 is indicated by a dotted line. Intersections of the FSC plots and FSC=0.143 is highlighted by an arrow together with the resolution estimates.
(E) Validation of the model vs map. FSC_{full} indicates FSC of the model against the full map. The difference between FSC_{work} and FSC_{free} is negligible, indicating no over fitting.

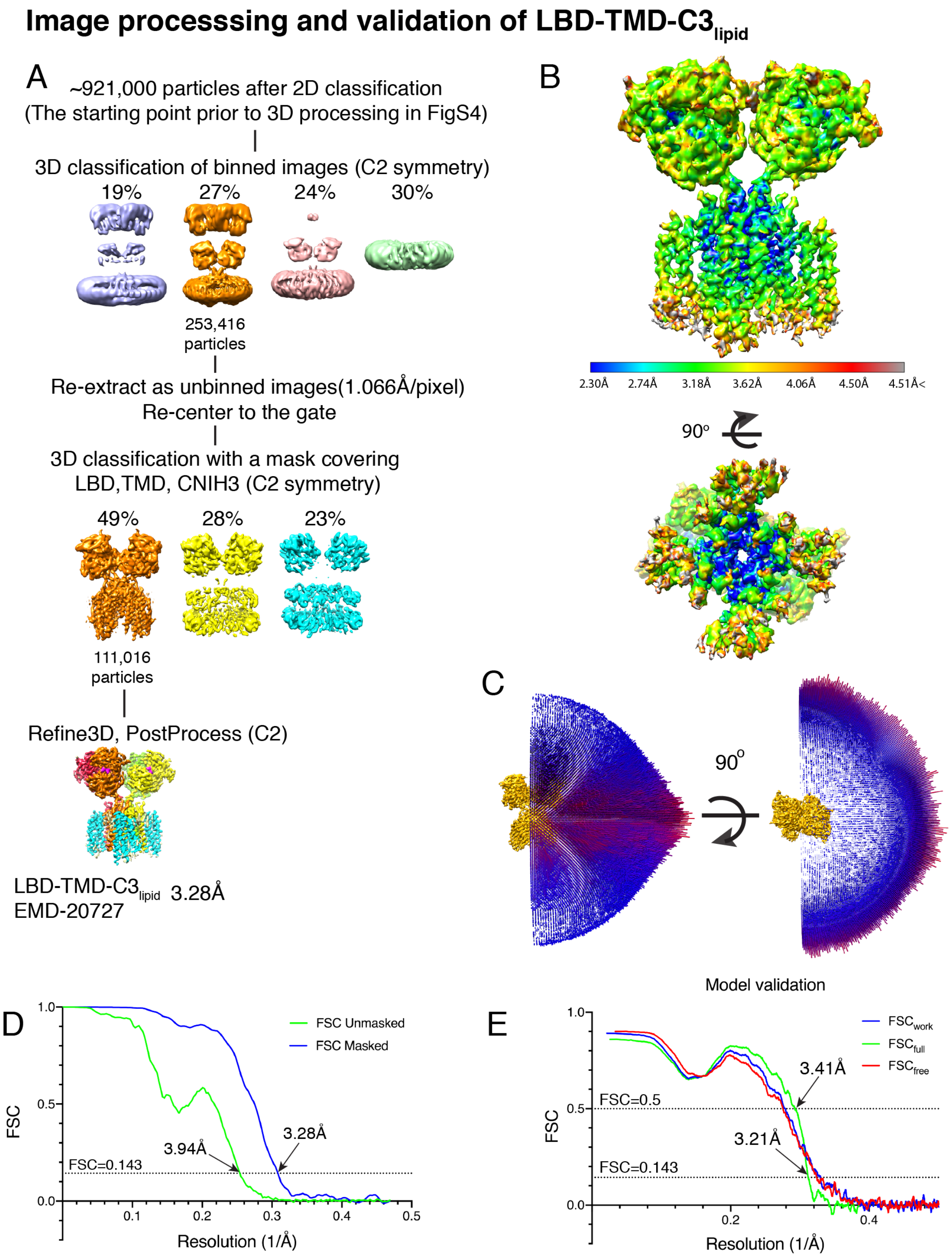

Figure S9. Angular distribution, local resolution, FSC curves, and model validation of the LBD-TMD-C3$_{\text{lipid}}$.

(A) Image processing workflow. C2 symmetry was imposed in all steps, including the initial 3D classification of the binned images. In the second step, focused classification and refinement was carried out using a mask excluding the NTD layer. This workflow produced a map with well-resolved lipid/detergent-like density surrounding the TMD and CNIH3 (see Material and Methods).

(B) Local resolution was calculated using ResMap. The color map indicates the resolution, which ranges between 2.3 to 4.5Å, the majority of the density is between 2.3 and 3.5Å.
(C) Distribution of the assigned angles of the particles that contributed to the final reconstruction. Excellent sampling of views for reconstruction is demonstrated.
(D) Fourier shell correlation (FSC) derived from half maps. FSC from masked maps and unmasked maps are shown. The position that corresponds to FSC=0.143 is indicated by a dotted line. Intersections of the FSC plots and FSC=0.143 is highlighted by an arrow together with the resolution estimates.
(E) Validation of the model vs map. FSC_{full} indicates FSC of the model against the full map. The difference between FSC_{work} and FSC_{free} is negligible, indicating no over fitting.

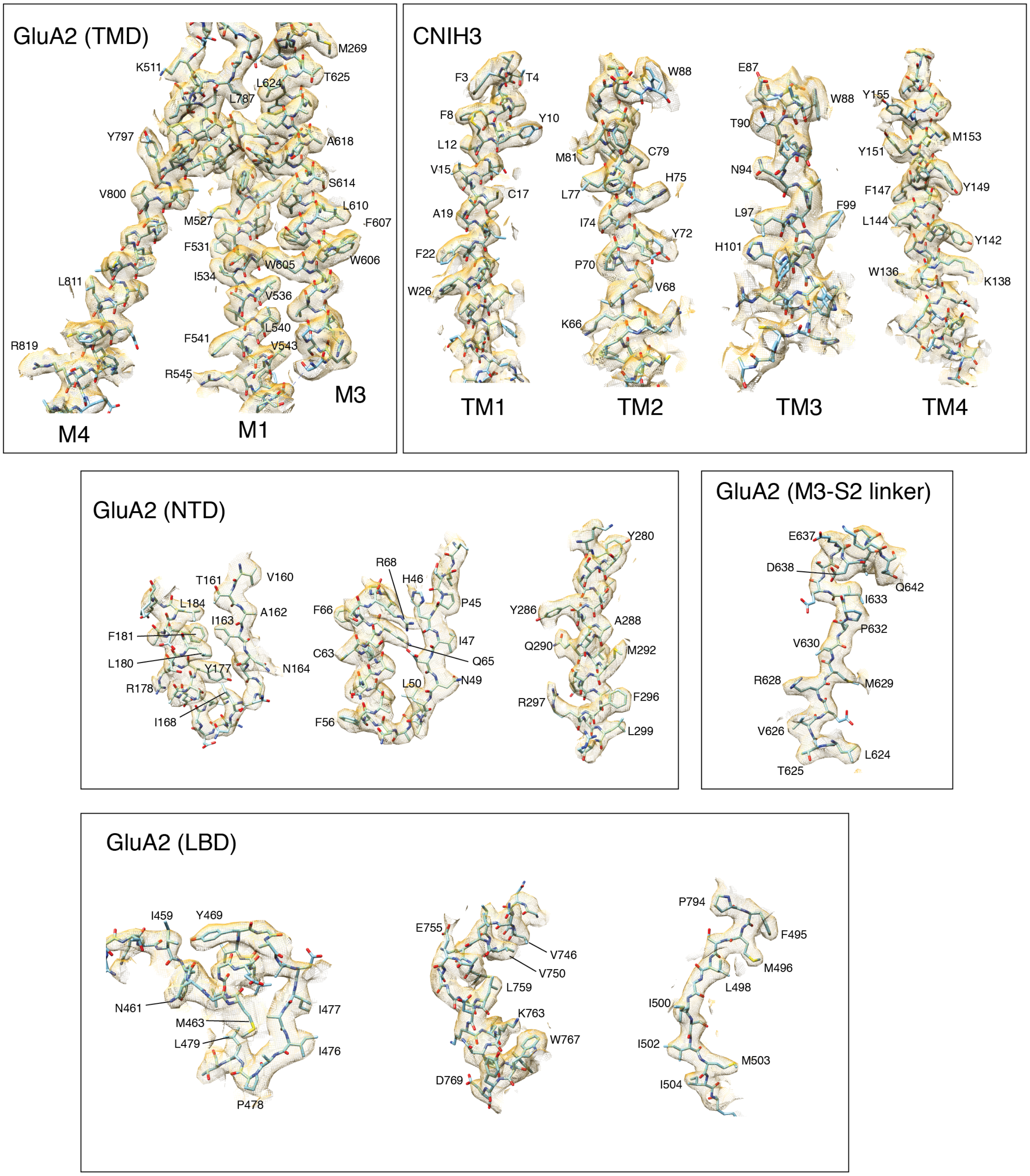

Figure S10. Representative sub-volumes of the density map and their fit against the model. The appearance of the map, which clearly resolves side chain and contour of the polypeptide backbone, is in agreement with the estimated overall resolution of 3~3.1Å. The sub-volumes of density maps, LBD-TMD-C3 and NTD(PS), are superimposed with their corresponding atomic models. The map and model is in good agreement.

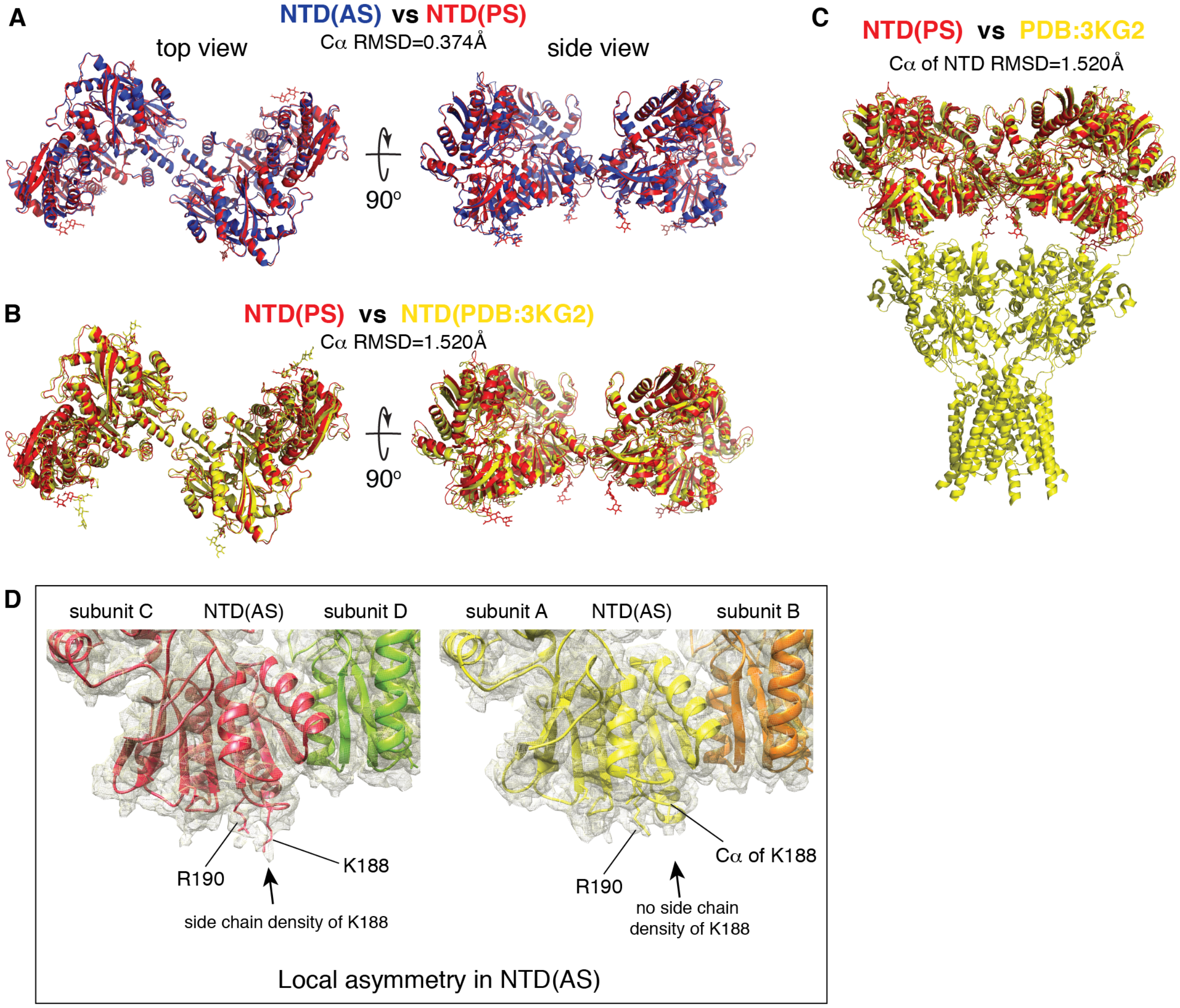

Figure S11. NTD architecture of A2-C3

(A) Superposition of models, NTD(AS) and NTD(PS). The alpha carbons of two models align at RMSD=0.374Å.

(B) Superposition of models, NTD(PS) and NTD from X-ray structure of the GluA2$_{cryst}$ tetramer bound to antagonist ZK200775 (PDB:3KG2). The alpha carbons of two models align at RMSD=1.520Å.

(C) Superposition of models, NTD(PS) and X-ray structure of the GluA2$_{cryst}$ tetramer bound to antagonist ZK200775 (PDB:3KG2). Note that the glycosylation at N241 of NTD(PS) is almost touching the LBDs of 3KG2. This is due to the construct design that has shorter NTD-LBD likner in 3KG2. As shown in Fig1C and H, the gap between the NTD and LBD is wide enough to accommodate glycosylation in A2-C3 in PS.

(D) Superposition of model and map in NTD(AS). The NTD dimers of CD subunits in AS is tilted downwards towards the LBD and make contact with LBD at K188 of C subunit (red). In contrast, the NTD dimer of AB subunits does not interact with LBD. The side chain density of K188 in A subunit is absent, whereas in C subunit it is well defined, creating a local asymmetry in K188 of AC subunits.

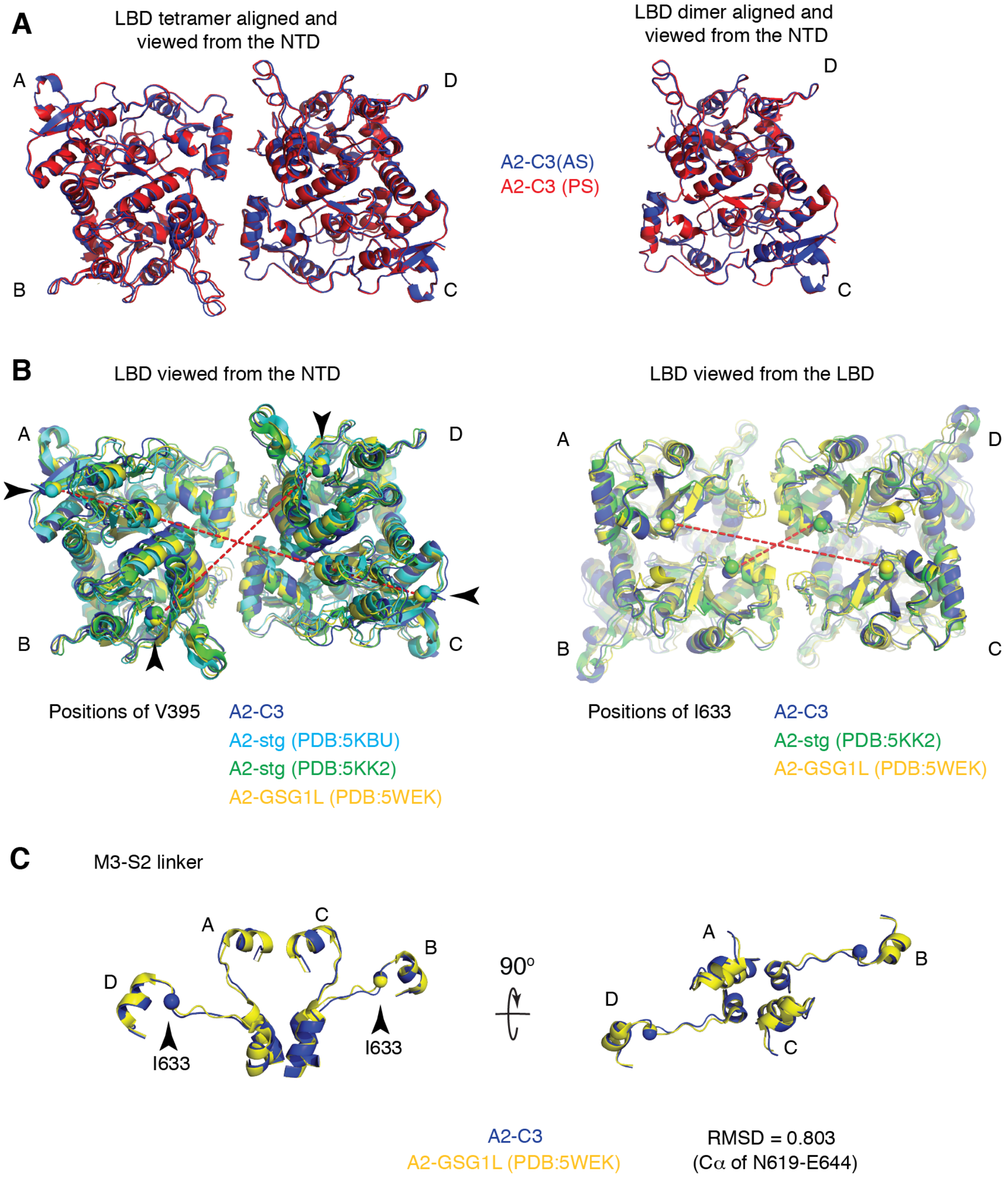

Figure S12. The LBD layer and M3-S2 linker of A2-C3

(A) The dimer-of-dimers architectures of LBDs of AS (blue) and PS (red) were virtually identical, alpha carbons of the two models align at RMSD=0.542Å (right). The alpha carbons of LBD dimer made of CD subunits of AS and PS align at RMSD=0.256Å (left).

(B) The dimer-of-dimers architectures of LBDs of various GluA2/auxiliary subunit complexes are very similar. V395 and I633 are shown as spheres. Average distances between V395 in AC and BD subunits (shown as red dashed lines) are 95.7Å and 53.25Å, respectively. Average distances between I633 in AC and BD subunits (shown as red dashed lines) are 51.6Å and 25.0Å, respectively.

(C) M3-S2 linker of A2-C3 and GluA2/GSG1L bound to ZK200775 were very similar. The alpha carbons of two structures align at RMSD=0.803Å.

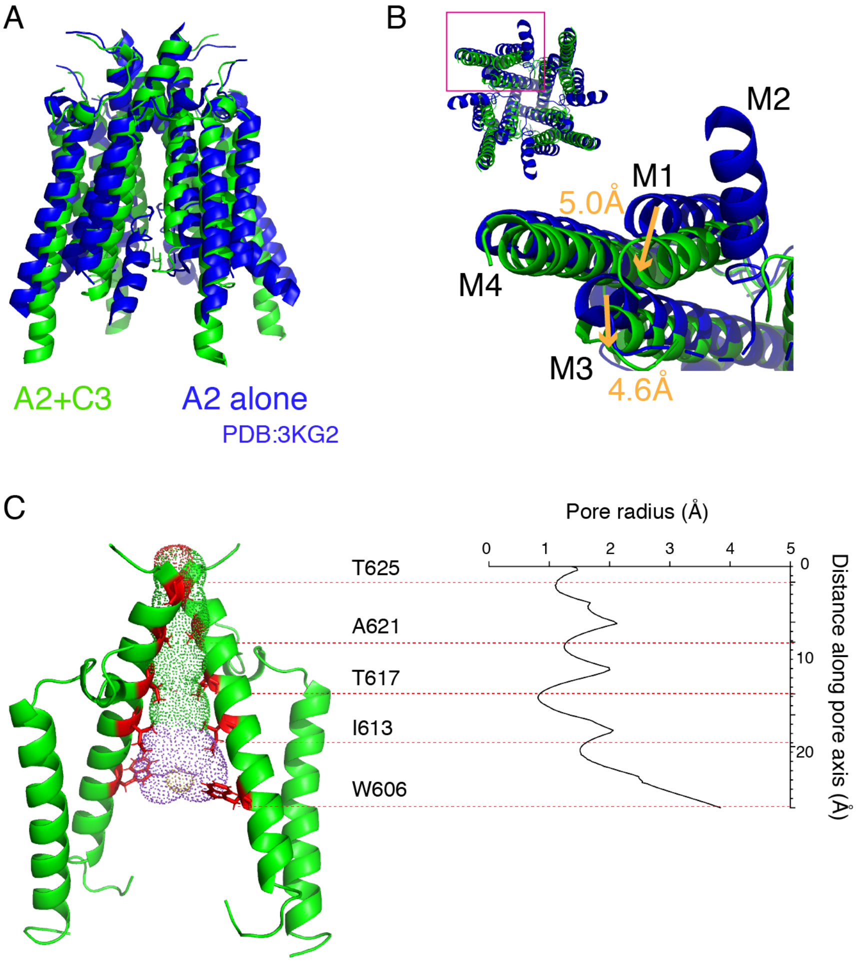

Figure S13. Architecture of the ion channel in the GluA2-CNIH3 complex.

(A) The TMD of GluA2/CNIH3 complex (green) and GluA2 alone (PDB:3KG2, blue) were compared. The CNIH3 is removed from the image for clarification. Both structures were bound to ZK200775. When the two structures were aligned using align function in PyMol (Version 2.0 Schrödinger, LLC), the pore gate formed of M3 and extracellular segments of M1 and M4 superimpose.

(B) The superimposed structures in (A) are viewed from the bottom. The red square in the left top inset is magnified. Compared to GluA2 alone, GluA2/CNIH3 complex adopts more compact architecture on the cytoplasmic side of the TMD. In the superimposed structures, excursion of F541 (M1) and G598 (M3) were 5.0Å and 4.6Å, respectively. The direction of the excursion is towards the center of the ion channel axis.

(C) The pore structure was analyzed using HOLE program. For clarity only the M3 and M1 of two subunits are shown. Resides T625, A621, T617, I613, and W606 are highlighted in red with side chains depicted. The pore diameter at each level along the pore axis was calculated by HOLE and displayed as a graph (right). The constriction is consistent with a closed channel.

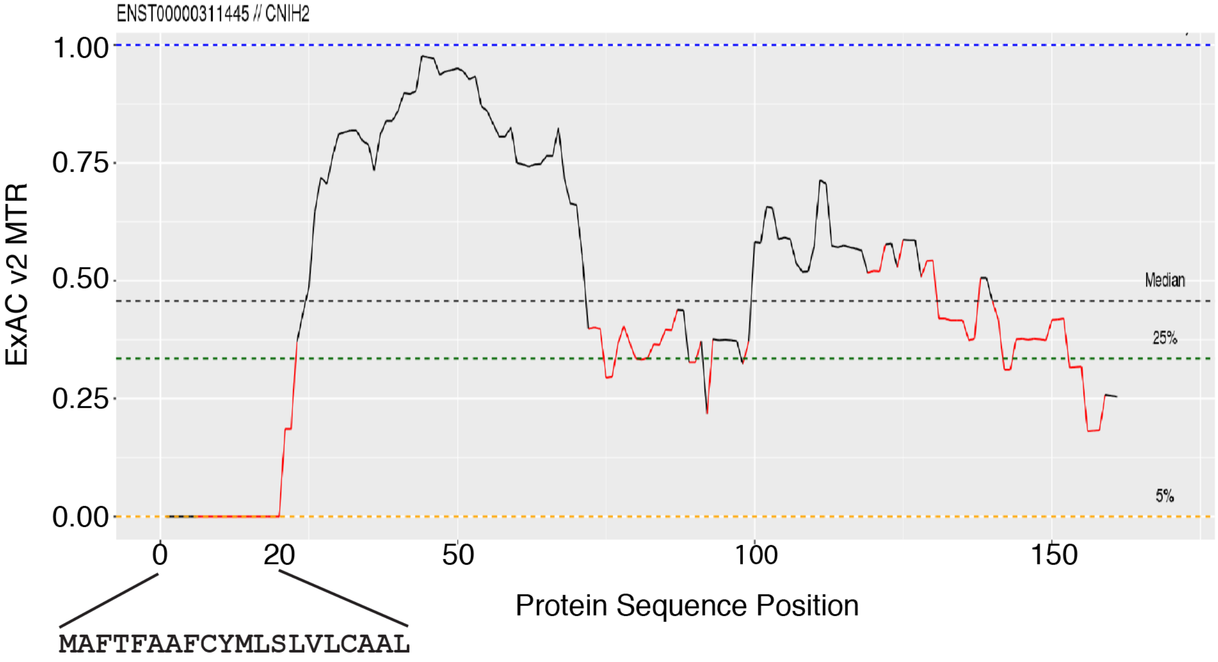

Figure S14. Missense tolerance ratio analysis of CNIH in human population.
CNIH2 was subject to missense tolerance ratio analysis using MTR Gene Viewer (http://mtr-viewer.mdhs.unimelb.edu.au). The first 20 amino acids at N-terminus are completely intolerant of mutation in the collection of over 150,000 human genome/exomes. This indicates that missense mutation in this region results in high probability of severe disease state, most likely lethal. Conversely the first 20 amino acids contain functionally critical sequence.

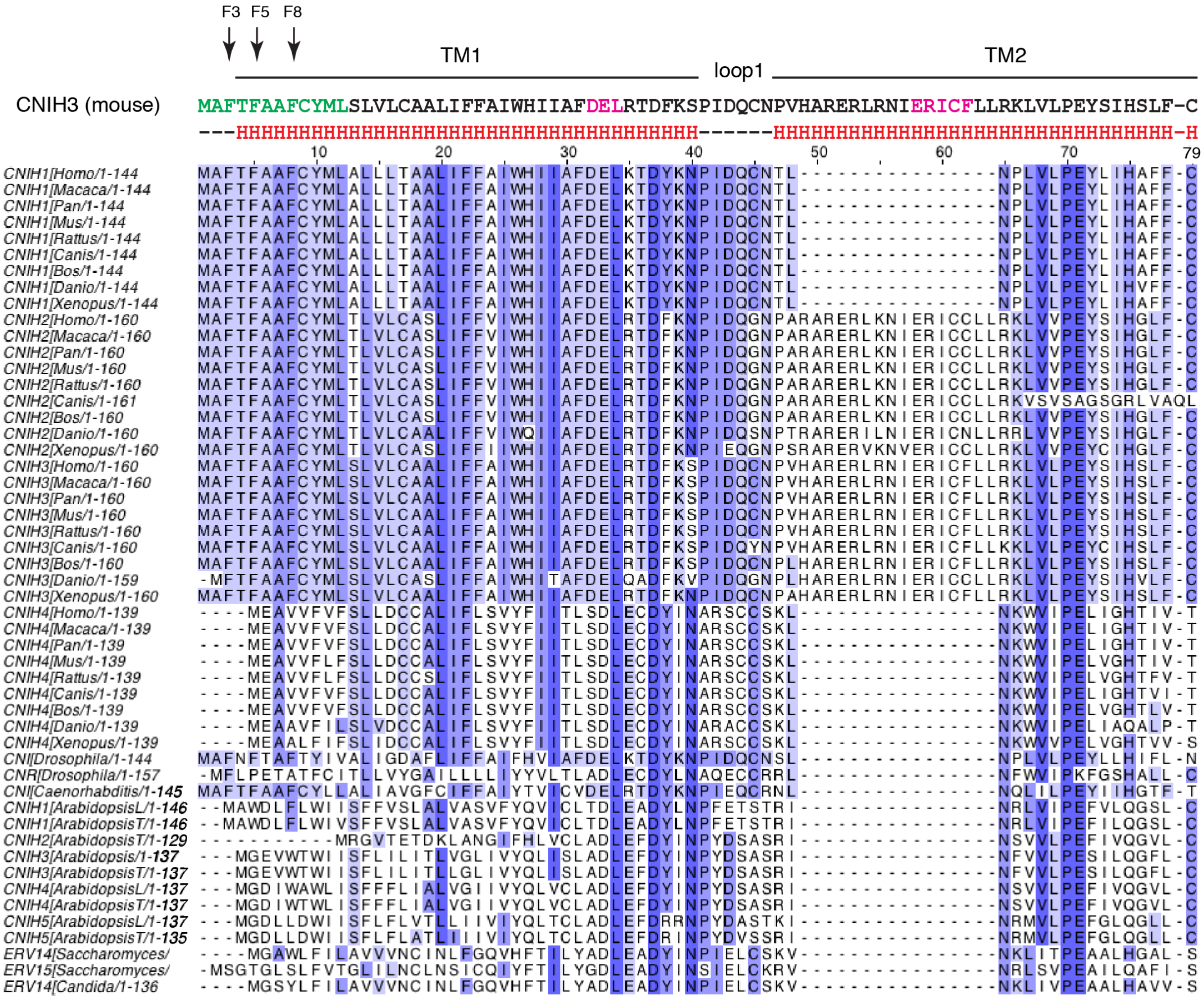

Figure S15a and S15b. Primary sequence and alignment of CNIH3 against its homologues. Primary and secondary structures of CNIH3 (top), and Clustal-Omega sequence alignment of cornichon homologues from various species (bottom) are shown across two pages. Top: red H indicates helices and blue E indicates sheets. The UMIP is highlighted in green. F3,5, and8 interacts with GluA2. W88 is conserved in all cornichons except for one species and is located at the hydrophobic loop between TM2 and TM3. M153 and L157 are two residues that interact with lipid like density L-f, which has characteristic feature of cholesterol group. The residues highlighted in magenta were shown in our previous study to partially attenuate gating modulation when mutated to alanines (*13*). Homo (Homo Sapiens), Macaca (Macaca mulatta), Pan (Pan troglodytes), Mus (Mus musculus), Rattus (Rattus norvegicus), Canis (Canis lupus familiaris), Bos (Bos Taurus), Danio (Danio rerio), Xenopus (Xenopus tropicalis), Drosophila (Drosophila melanogaster), Caenorhabditis (Caenorhabditis elegans), ArabidopsisL (Arabidopsis lyrata subsp. Lyrata), ArabidopsisT (Arabidopsis thaliana), Saccharomyces (Saccharomyces cerevisiae), Candida (Candida glabrata). The color intensity in the columns indicates magnitude of identity across species, i.e. stronger the blue higher the identity.

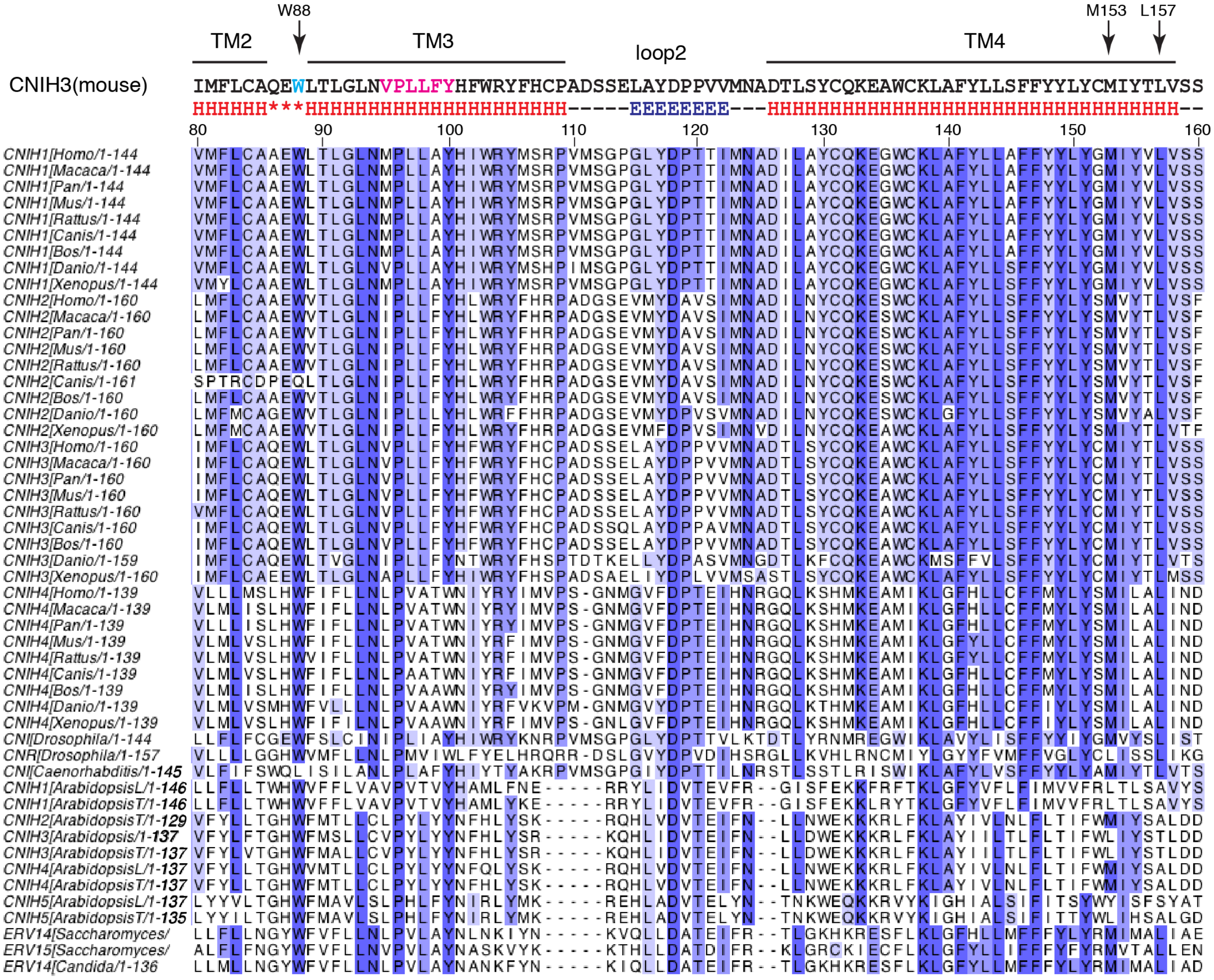

```
CNIH3(mouse)                 IMFLCAQEWLTLGLNVPLLFYHFWRYFHCPADSSELAYDPPVVMNADTLSYCQKEAWCKLAFYLLSFFYYLYCMIYTLVSS
                             HHHHHH***HHHHHHHHHHHHHHHHHHHHH-----EEEEEEEE---HHHHHHHHHHHHHHHHHHHHHHHHHHHHHHHHH--
CNIH1[Homo/1-144             VMFLCAAEWLTLGLNMPLLAYHIWRYMSRPVMSGPGLYDPTTIMNADILAYCQKEGWCKLAFYLLAFFYYLYGMIYVLVSS
CNIH1[Macaca/1-144           VMFLCAAEWLTLGLNMPLLAYHIWRYMSRPVMSGPGLYDPTTIMNADILAYCQKEGWCKLAFYLLAFFYYLYGMIYVLVSS
CNIH1[Pan/1-144              VMFLCAAEWLTLGLNMPLLAYHIWRYMSRPVMSGPGLYDPTTIMNADILAYCQKEGWCKLAFYLLAFFYYLYGMIYVLVSS
CNIH1[Mus/1-144              VMFLCAAEWLTLGLNMPLLAYHIWRYMSRPVMSGPGLYDPTTIMNADILAYCQKEGWCKLAFYLLAFFYYLYGMIYVLVSS
CNIH1[Rattus/1-144           VMFLCAAEWLTLGLNMPLLAYHIWRYMSRPVMSGPGLYDPTTIMNADILAYCQKEGWCKLAFYLLAFFYYLYGMIYVLVSS
CNIH1[Canis/1-144            VMFLCAAEWLTLGLNMPLLAYHIWRYMSRPVMSGPGLYDPTTIMNADILAYCQKEGWCKLAFYLLAFFYYLYGMIYVLVSS
CNIH1[Bos/1-144              VMFLCAAEWLTLGLNMPLLAYHIWRYMSRPVMSGPGLYDPTTIMNADILAYCQKEGWCKLAFYLLAFFYYLYGMIYVLVSS
CNIH1[Danio/1-144            VMFLCAAEWLTLGLNVPLLAYHIWRYMSHPIMSGPGLYDPTTIMNADILAYCQKEGWCKLAFYLLSFFYYLYGMIYVLVSS
CNIH1[Xenopus/1-144          VMYLCAAEWLTLGLNMPLLAYHIWRYMSRPVMSGPGLYDPTTIMNADILAYCQKEGWCKLAFYLLSFFYYLYGMIYVLVSS
CNIH2[Homo/1-160             LMFLCAAEWVTLGLNIPLLFYHLWRYFHRPADGSEVMYDAVSIMNADILNYCQKESWCKLAFYLLSFFYYLYSMVYTLVSF
CNIH2[Macaca/1-160           LMFLCAAEWVTLGLNIPLLFYHLWRYFHRPADGSEVMYDAVSIMNADILNYCQKESWCKLAFYLLSFFYYLYSMVYTLVSF
CNIH2[Pan/1-160              LMFLCAAEWVTLGLNIPLLFYHLWRYFHRPADGSEVMYDAVSIMNADILNYCQKESWCKLAFYLLSFFYYLYSMVYTLVSF
CNIH2[Mus/1-160              LMFLCAAEWVTLGLNIPLLFYHLWRYFHRPADGSEVMYDAVSIMNADILNYCQKESWCKLAFYLLSFFYYLYSMVYTLVSF
CNIH2[Rattus/1-160           LMFLCAAEWVTLGLNIPLLFYHLWRYFHRPADGSEVMYDAVSIMNADILNYCQKESWCKLAFYLLSFFYYLYSMVYTLVSF
CNIH2[Canis/1-161            SPTRCDPEQLTLGLNIPLLFYHLWRYFHRPADGSEVMYDAVSIMNADILNYCQKESWCKLAFYLLSFFYYLYSMVYTLVSF
CNIH2[Bos/1-160              LMFLCAAEWVTLGLNIPLLFYHLWRYFHRPADGSEVMYDAVSIMNADILNYCQKESWCKLAFYLLSFFYYLYSMVYTLVSF
CNIH2[Danio/1-160            LMFMCAGEWVTLGLNIPLLLYHLWRFFHRPADGSEVMYDPVSVMNADILNYCQKESWCKLGFYLLSFFYYLYSMVYALVSF
CNIH2[Xenopus/1-160          LMFMCAAEWVTLGLNIPLLFYHLWRYFHRPADGSEVMFDPVSIMNVDILNYCQKEAWCKLAFYLLSFFYYLYSMIYTLVTF
CNIH3[Homo/1-160             IMFLCAQEWLTLGLNVPLLFYHFWRYFHCPADSSELAYDPPVVMNADTLSYCQKEAWCKLAFYLLSFFYYLYCMIYTLVSS
CNIH3[Macaca/1-160           IMFLCAQEWLTLGLNVPLLFYHFWRYFHCPADSSELAYDPPVVMNADTLSYCQKEAWCKLAFYLLSFFYYLYCMIYTLVSS
CNIH3[Pan/1-160              IMFLCAQEWLTLGLNVPLLFYHFWRYFHCPADSSELAYDPPVVMNADTLSYCQKEAWCKLAFYLLSFFYYLYCMIYTLVSS
CNIH3[Mus/1-160              IMFLCAQEWLTLGLNVPLLFYHFWRYFHCPADSSELAYDPPVVMNADTLSYCQKEAWCKLAFYLLSFFYYLYCMIYTLVSS
CNIH3[Rattus/1-160           VMFLCAQEWLTLGLNVPLLFYHFWRYFHCPADSSELAYDPPVVMNADTLSYCQKEAWCKLAFYLLSFFYYLYCMIYTLVSS
CNIH3[Canis/1-160            IMFLCAQEWLTLGLNVPLLFYHFWRYFHCPADSSQLAYDPPAVMNADTLSYCQKEAWCKLAFYLLSFFYYLYCMIYTLVSS
CNIH3[Bos/1-160              IMFLCAQEWLTLGLNVPLLFYHFWRYFHCPADSSELAYDPPVVMNADTLSYCQKEAWCKLAFYLLSFFYYLYCMIYTLVSS
CNIH3[Danio/1-159            IMFLCAQEWLTVGLNIPLLFYNTWRYFHSPTDTKELLYDPASVMNGDTLKFCQKEAWCKMSFFVLSFFYYLYCMIYTLVTS
CNIH3[Xenopus/1-160          IMFLCAEEWLTLGLNAPLLFYHIWRYFHSPADSAELIYDPLVVMSASTLSYCQKEAWCKLAFYLLSFFYYLYCMIYTLMSS
CNIH4[Homo/1-139             VLLLMSLHWFIFLLNLPVATWNIYRYIMVPS-GNMGVFDPTEIHNRGQLKSHMKEAMIKLGFHLLCFFMYLYSMILALIND
CNIH4[Macaca/1-139           VLMLISLHWFIFLLNLPVATWNIYRYIMVPS-GNMGVFDPTEIHNRGQLKSHMKEAMIKLGFHLLCFFMYLYSMILALIND
CNIH4[Pan/1-139              VLLLISLHWFIFLLNLPVATWNIYRYIMVPS-GNMGVFDPTEIHNRGQLKSHMKEAMIKLGFHLLCFFMYLYSMILALIND
CNIH4[Mus/1-139              VLMLVSLHWFIFLLNLPVATWNIYRFIMVPS-GNMGVFDPTEIHNRGQLKSHMKEAMIKLGFYLLCFFMYLYSMILALIND
CNIH4[Rattus/1-139           VLMLVSLHWVIFLLNLPVATWNIYRFIMVPS-GNMGVFDPTEIHNRGQLKSHMKEAMIKLGFYLLCFFMYLYSMILALIND
CNIH4[Canis/1-139            VLMLVSLHWFIFLLNLPAATWNIYRFIMVPS-GNMGVFDPTEIHNRGQLKSHMKEAMIKLGFHLLCFFMYLYSMILALIND
CNIH4[Bos/1-139              VLMLISLHWFIFLLNLPVAAWNIYRYIMVPS-GNMGVFDPTEIHNRGQLKSHMKEAMIKLGFHLLCFFMYLYSMILALIND
CNIH4[Danio/1-139            VLMLVSMHWFVLLLNLPVAAWNIYRFVKVPM-GNMGVYDPTEIHNRGQLKTHMKEAMIKLGFHLLCFFIYLYSMILALIND
CNIH4[Xenopus/1-139          VLMLVSLHWFIFILNLPVAAWNIYRFIMVPS-GNLGVFDPTEIHNRGQLKSHMKEAMIKLGFHLLCFFIYLYSMILALIND
CNI[Drosophila/1-144         LLFLFCGEWFSLCINIPLIAYHIWRYKNRPVMSGPGLYDPTTVLKTDTLYRNMREGWIKLAVYLISFFYYIYGMVYSLIST
CNR[Drosophila/1-157         VLLLLGGHWVMFLLNLPMVIWLFYELHRQRR-DSLGVYDPVDIHSRGLLKVHLRNCMIYLGYYFVMFFVGLYCLISSLIKG
CNI[Caenorhabditis/1-145     VLFIFSWQLISILANLPLAFYHIYTYAKRPVMSGPGIYDPTTILNRSTLSSTLRISWIKLAFYLVSFFYYLYAMIYTLVTS
CNIH1[ArabidopsisL/1-146     LLFLLTWHWVFFLVAVPVTVYHAMLFNE-----RRYLIDVTEVFR--GISFEKKFRFTKLGFYVFLFIMVVFRLTLSAVYS
CNIH1[ArabidopsisT/1-146     LLFLLTWHWVFFLVAVPVTVYHAMLYKE-----RRYLIDVTEVFR--GISFEKKLRYTKLGFYVFLFIMVVFRLTLSAVYS
CNIH2[ArabidopsisT/1-129     VFYLLTGHWFMTLLCLPYLYYNFHLYSK-----RQHLVDVTEIFN--LLNWEKKKRLFKLAYIVLNLFLTIFWMIYSALDD
CNIH3[Arabidopsis/1-137      VFYLFTGHWFMSLLCVPYLYYNFHLYSR-----KQHLIDVTEIFN--LLDWEKKKRLFKLAYIILTLFLTIFWLIYSTLDD
CNIH3[ArabidopsisT/1-137     VFYLVTGHWFMALLCVPYLYYNFHLYSR-----KQHLIDVTEIFN--LLDWEKKKRLFKLAYIILTLFLTIFWLIYSTLDD
CNIH4[ArabidopsisL/1-137     VFYLLTGHWVMTLLCLPYLYYNFQLYSK-----RQHLVDVTEIFN--LLNWEKKKRLFKLAYIVLNLFLTIFWMIYSALDD
CNIH4[ArabidopsisT/1-137     VFYLLTGHWFMTLLCLPYLYYNFHLYSK-----RQHLVDVTEIFN--LLNWEKKKRLFKLAYIVLNLFLTIFWMIYSALDD
CNIH5[ArabidopsisL/1-137     LYYVLTGHWFMAVLSLPHLFYNIRLYMK-----REHLADVTELYN--TNKWEQKKRVYKIGHIALSIFITSYWYISFSYAT
CNIH5[ArabidopsisT/1-135     LYYILTGHWFMAVLSLPHLFYNIRLYMK-----REHLADVTELYN--TNKWEQKKRVYKIGHIALSIFITTYWLIHSALGD
ERV14[Saccharomyces/         LLFLLNGYWFVFLLNLPVLAYNLNKIYN-----KVQLLDATEIFR--TLGKHKRESFLKLGFHLLMFFFYLYRMIMALIAE
ERV15[Saccharomyces/         ALFLFNGYWFVFLLNVPVLAYNASKVYK-----KTHLLDATDIFR--KLGRCKIECFLKLGFYLLIFFFYFYRMVTALLEN
ERV14[Candida/1-136          LLMLLNGYWFVFLLNLPVLAYNANKFYN-----KIQLLDATEIFR--TLGKHKRESFLKLGFYLLMFFFYLYRMIMALIAD
```

Figure S15b (Continued from previous page)

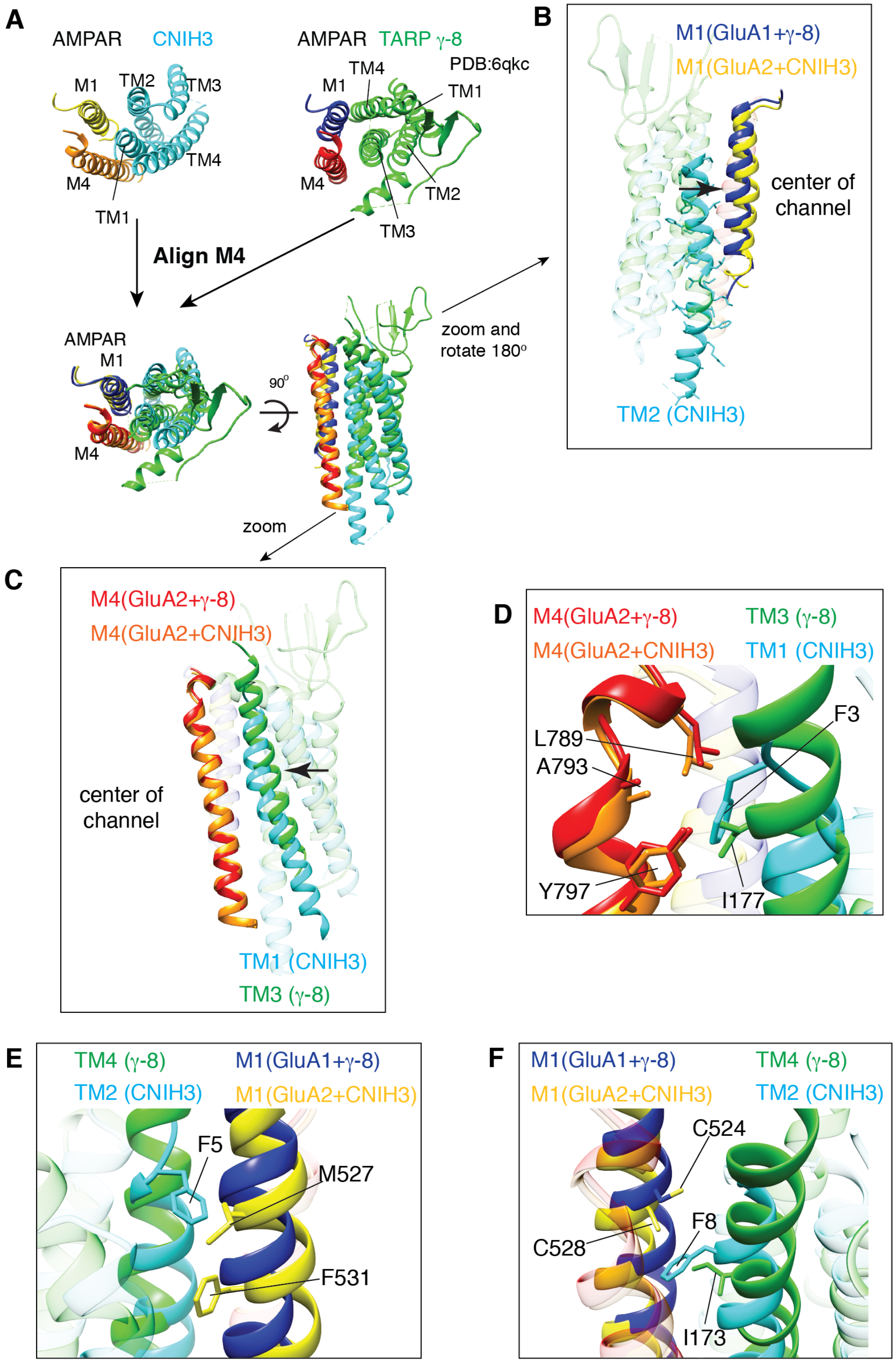

Figure S16. Interaction interface of A2-C3 vs AMPAR/TARP γ-8

(A) Fig2D is replicated for clarity to introduce panels B-F. The M1 and M4 of adjacent subunits of AMPAR form the binding surface for both CNIH3 and TARP. By only aligning M4 helix, the remaining helices (M1, and TM1-4 of CNIH3 or TARP γ-8) were superimposed. The models before alignment are shown on the top.

(B) TM2 of CNIH3 pushes M1 inward towards the center of the channel (arrow). Note that M4 is aligned, and thus the difference in the position of M1 is relative to M4.
(C) TM1 of CNIH3 bends towards M4 (arrow) and makes extensive contact with M4, compared to TM3 of γ-8.
(D) The side chain F3 of CNIH3 and I177 of γ-8 occupy similar space at the interaction interface, and thus may interact with similar residues on M4 of GluA2. However, given the difference in the size of the side chain between F and I, L789 and A793 may not interact with I177.
(E) No side chain in γ-8 serves as a counterpart of F5 of CNIH3 at the interaction interface.
(F) The side chain F3 of CNIH3 and I173 of γ-8 partially occupy the same space at the interaction interface, but unlikely to interact with AMPAR in the same way. Note that C528 of GluA2 corresponds to C524 of GluA1, and these residues point different directions.

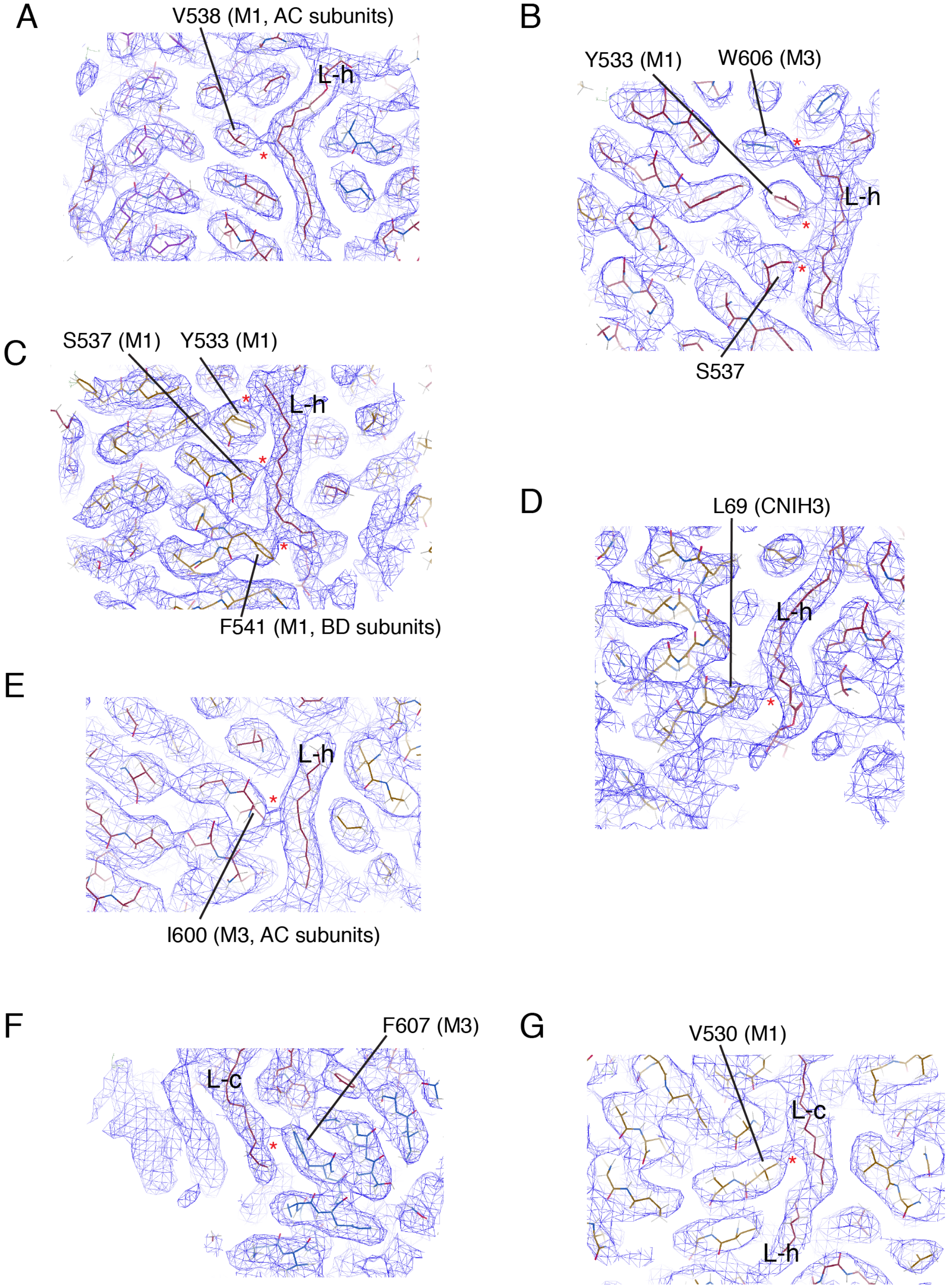

Figure S17. Contacts between lipid-like densities and side chains.
Sections of superimposed density map and model. Sections were taken at slices that reveal contacts between lipid-like densities and protein residues. Snapshots of sections were taken in Coot (*19*). Contacts are highlighted by red asterisks.

(A) The contact made between V538 (M1) of GluA2 and L-h. The interaction only occurs in the A and C subunits in the tetrameric assembly.

(B) Y533 (M1), S537 (M1) and W606 (M3) of GluA2 interacts with L-h. The interaction occurs in all subunits in the tetrameric assembly.

(C) Similar to (B) contacts between L-h and Y533 (M1) and S537 (M1) are shown. In addition, in this view the interaction between F541 (M1) with L-h is shown. The latter interaction occurs only in the B and D subunits in the tetrameric assembly.

(D) The contact made between L69 (TM2) of CNIH3 and L-h.

(E) The contact made between I600 (M3) of GluA2 and L-h. The interaction occurs only in the A and C subunits in the tetrameric assembly.

(F) The contact made between F607 (M3) of GluA2 and L-c.

(G) The contact made between V530 (M1) of GluA2 and L-c.

A

Position in CNIH3	Position in GluA2	Cα distance (Å)
A2	A793	9.3
F3	A793	7.5
F3	L789	7.6
F5	C528	6.1
F5	M527	7.7
F8	C528	7.2

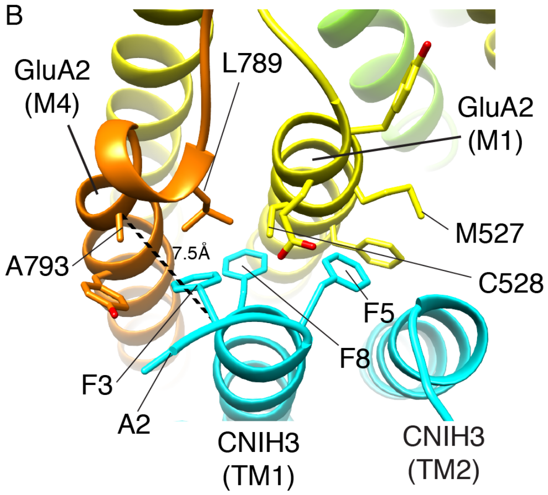

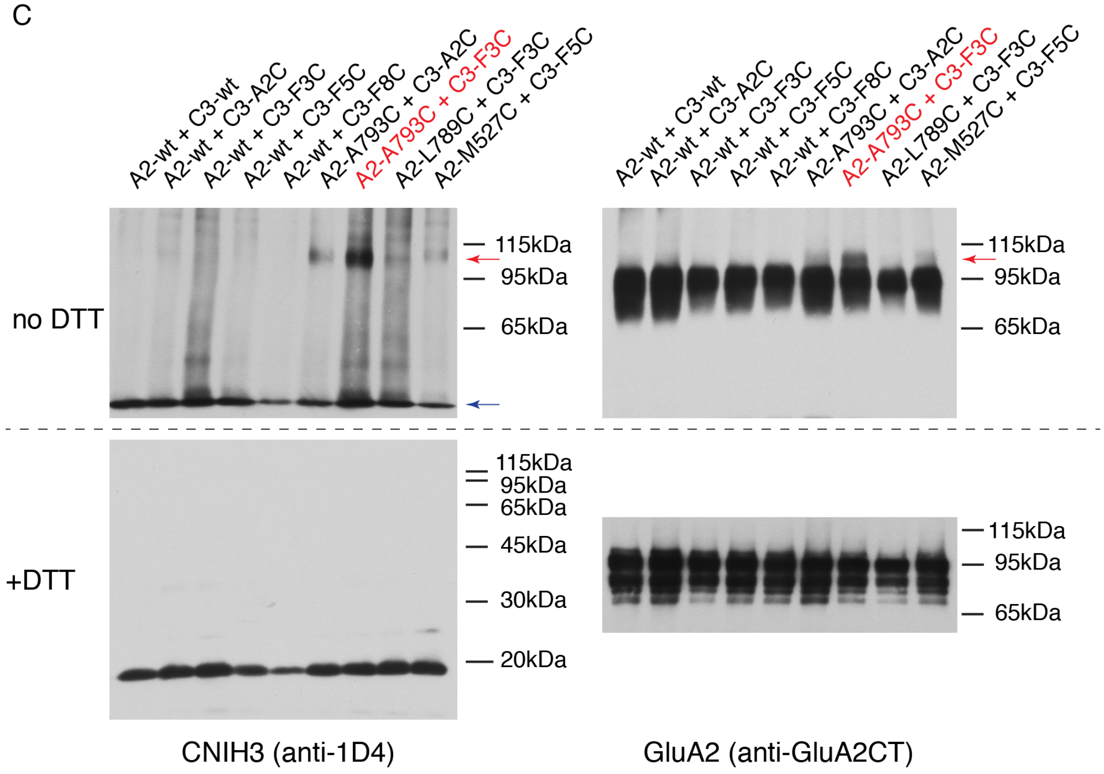

Figure 18S. Cysteine crosslinking between nearby residues in A2-C3 structure
(A) A table summarizing distances between residues that are nearby at the interface between GluA2 and CNIH3.
(B) Interaction interface between GluA2 and CNIH3. The dashed line connects the alpha carbons of A793 and F3, whose distance is 7.5Å.
(C) Western blots of GluA2/CNIH3 complexes. The samples were either reduced by DTT (+DTT) or untreated (no DTT) prior to SDS-PAGE. The loaded samples are labeled at the top of each lane. Each complex was enriched by batch immuno-affinity purification from the lysate of HEK cells transfected with a plasmid that co-expresses the corresponding variants of GluA2 and CNIH3 (see Methods). Red arrows indicate the mobility of disulfide cross-linked GluA2-CNIH3 complex. Crosslinked bands were observed at the identical mobility in both anti-GluA2 and anti-

1D4 blots. The blue arrow indicates the position of free CNIH3 at the dye front. Under non-reducing condition, a robust crosslinking was detectable between A793C of GluA2 and F3C of CNIH3. Crosslinked band was absent when the samples were pre-treated with DTT. Weaker crosslinking was detectable in other constructs. I suggest that weak crosslinking between A793C and A2C occurred, despite longer distances in the cryo-EM structure, because substitution to cysteine altered the folding. No crosslinking was detectable in any combination that contained the wild type.

TableS1. Cryo-EM data collection, refinement, and validation statistics.

Cryo-EM map	**NTD(AS)**	**NTD(PS)**	**LBD-TMD-C3**	**LBD-TMD-C3 (AS) I**	**LBD-TMD-C3 (AS) II**	**LBD-TMD-C3 (PS)**	**LBD-TMD-C3$_{lipid}$**	**A2-C3 (AS)**	**A2-C3 (PS)**
EMD accession	**20666**	**20654**	**20330**	**20732**	**20733**	**20734**	**20727**	**20717**	**20332**
PDB accession	**6U6I**	**6U5S**	**6PEQ**		**6UD4**	**6UD8**	**6UCB**		
Data collection and image processing									
Microscope	Thermo Fisher Titan Krios								
Detector	BioQuantum K3								
Magnification	81,000x								
Acceleration voltage (keV)	300								
Total electron exposure	58.5								
Defocus range (µm)	-0.8 to -2.0								
Pixel size (Å/pixel)	1.066							2.132	
Symmetry imposed	C1	C2	C2	C1	C2	C2	C2	C1	C1
Number of micrographs	11,340								
Initial model	EMD-2680								
Final particle images	84,225	121,778	188,982	84,584		76,689	111,016	218,413	190,470
Map resolution (Å)	3.1	3.1	3.0	3.5	3.3	3.2	3.3	4.4	4.4
FSC threshold	0.143								
Refinement									
Model resolution (Å)	3.5	3.4	3.4		3.7	3.5	3.4		
FSC threshold	0.5								
Map sharpening B factor (Å^2)	-43.3	-54.0	-50.3	-41.1	-49.3	-42.6	-92.1	-117	-114
Model composition									
Non-hydrogen atoms (#)	11,364	11,706	16,326		16,172	16,180	16,630		
Protein residues (#)	1496	1504	2,044		2,044	2,044	2,044		
Ligands (PDB code: #)	BMA:2, NAG:9	BMA:4, NAG:16	OLC:8, ZK1:4, CLR:4, PAM:14		OLC:4, ZK1:4, CLR:4	OLC:4, ZK1:4, CLR:4	OLC:8, ZK1:4, CLR:4, PAM:14		

Table S1. (Continued from previous page)

Cryo-EM map	**NTD(AS)**	**NTD(PS)**	**LBD-TMD-C3**	**LBD-TMD-C3 (AS) I**	**LBD-TMD-C3 (AS) II**	**LBD-TMD-C3 (PS)**	**LBD-TMD-$C3_{lipid}$**	**A2-C3 (AS)**	**A2-C3 (PS)**
RMS deviations									
Bond lengths (Å)	0.004	0.003	0.003		0.003	0.003	0.003		
Bond angles (^{o})	0.492	0.942	0.593		0.562	0.766	0.498		
Validation									
MolProbity score	1.58	1.22	1.44		1.44	1.47	1.35		
Clashscore	3.18	2.32	2.65		2.90	2.96	2.22		
Poor rotamers (%)	0.00	0.00	0.00		0.12	0.00	0.00		
Ramachandran plot									
Favored (%)	92.41	96.66	94.34		94.84	94.39	94.94		
Allowed (%)	7.59	3.34	5.66		5.16	5.61	5.06		
Disallowed (%)	0.00	0.00	0.00		0.00	0.00	0.00		

References

1. T. Nakagawa, Y. Cheng, E. Ramm, M. Sheng, T. Walz, Structure and different conformational states of native AMPA receptor complexes. *Nature* **433**, 545-549 (2005).
2. Y. Zhao, S. Chen, C. Yoshioka, I. Baconguis, E. Gouaux, Architecture of fully occupied GluA2 AMPA receptor-TARP complex elucidated by cryo-EM. *Nature* **536**, 108-111 (2016).
3. A. I. Sobolevsky, M. P. Rosconi, E. Gouaux, X-ray structure, symmetry and mechanism of an AMPA-subtype glutamate receptor. *Nature* **462**, 745-756 (2009).
4. J. R. Meyerson *et al.*, Structural mechanism of glutamate receptor activation and desensitization. *Nature*, (2014).
5. T. Nakagawa, Y. Cheng, M. Sheng, T. Walz, Three-dimensional structure of an AMPA receptor without associated stargazin/TARP proteins. *Biol Chem* **387**, 179-187 (2006).
6. E. C. Twomey, M. V. Yelshanskaya, R. A. Grassucci, J. Frank, A. I. Sobolevsky, Channel opening and gating mechanism in AMPA-subtype glutamate receptors. *Nature*, (2017).
7. S. Chen *et al.*, Activation and Desensitization Mechanism of AMPA Receptor-TARP Complex by Cryo-EM. *Cell* **170**, 1234-1246 e1214 (2017).
8. B. Herguedas *et al.*, Architecture of the heteromeric GluA1/2 AMPA receptor in complex with the auxiliary subunit TARP gamma8. *Science* **364**, (2019).
9. M. V. Yelshanskaya, M. Li, A. I. Sobolevsky, Structure of an agonist-bound ionotropic glutamate receptor. *Science* **345**, 1070-1074 (2014).
10. N. M. Hawken, E. I. Zaika, T. Nakagawa, Engineering defined membrane-embedded elements of AMPA receptor induces opposing gating modulation by cornichon 3 and stargazin. *J Physiol*, (2017).
11. I. D. Coombs *et al.*, Cornichons modify channel properties of recombinant and glial AMPA receptors. *J Neurosci* **32**, 9796-9804 (2012).
12. K. K. Ogden, S. F. Traynelis, Contribution of the M1 transmembrane helix and pre-M1 region to positive allosteric modulation and gating of N-methyl-D-aspartate receptors. *Mol Pharmacol* **83**, 1045-1056 (2013).
13. N. F. Shanks *et al.*, Molecular Dissection of the Interaction between the AMPA Receptor and Cornichon Homolog-3. *J Neurosci* **34**, 12104-12120 (2014).
14. A. N. Farina *et al.*, Separation of domain contacts is required for heterotetrameric assembly of functional NMDA receptors *Journal of Neuroscience*, (2011).
15. N. F. Shanks, T. Maruo, A. N. Farina, M. H. Ellisman, T. Nakagawa, Contribution of the global subunit structure and stargazin on the maturation of AMPA receptors. *J Neurosci* **30**, 2728-2740 (2010).
16. J. Zivanov *et al.*, New tools for automated high-resolution cryo-EM structure determination in RELION-3. *Elife* **7**, (2018).
17. S. Q. Zheng *et al.*, MotionCor2: anisotropic correction of beam-induced motion for improved cryo-electron microscopy. *Nat Methods* **14**, 331-332 (2017).
18. A. Rohou, N. Grigorieff, CTFFIND4: Fast and accurate defocus estimation from electron micrographs. *J Struct Biol* **192**, 216-221 (2015).
19. P. Emsley, B. Lohkamp, W. G. Scott, K. Cowtan, Features and development of Coot. *Acta Crystallogr D Biol Crystallogr* **66**, 486-501 (2010).

20. A. Drozdetskiy, C. Cole, J. Procter, G. J. Barton, JPred4: a protein secondary structure prediction server. *Nucleic Acids Res* **43**, W389-394 (2015).
21. P. V. Afonine *et al.*, Real-space refinement in PHENIX for cryo-EM and crystallography. *Acta Crystallogr D Struct Biol* **74**, 531-544 (2018).
22. S. Masiulis *et al.*, GABAA receptor signalling mechanisms revealed by structural pharmacology. *Nature* **565**, 454-459 (2019).
23. D. Soto, I. D. Coombs, E. Gratacos-Batlle, M. Farrant, S. G. Cull-Candy, Molecular Mechanisms Contributing to TARP Regulation of Channel Conductance and Polyamine Block of Calcium-Permeable AMPA Receptors. *J Neurosci* **34**, 11673-11683 (2014).
24. N. F. Shanks *et al.*, Differences in AMPA and kainate receptor interactomes facilitate identification of AMPA receptor auxiliary subunit GSG1L. *Cell Rep* **1**, 590-598 (2012).